



Publication Year	2017
Acceptance in OA	2020-08-27T09:38:31Z
Title	The history of chemical enrichment in the intracluster medium from cosmological simulations
Authors	BIFFI, Veronica, Planelles, S., BORGANI, STEFANO, Fabjan, D., RASIA, ELENA, MURANTE, Giuseppe, TORNATORE, Luca, Dolag, K., GRANATO, Gian Luigi, GASPARI, MASSIMO, Beck, A. M.
Publisher's version (DOI)	10.1093/mnras/stx444
Handle	http://hdl.handle.net/20.500.12386/26867
Journal	MONTHLY NOTICES OF THE ROYAL ASTRONOMICAL SOCIETY
Volume	468

The history of chemical enrichment in the intracluster medium from cosmological simulations

V. Biffi,^{1,2★} S. Planelles,³ S. Borgani,^{1,2,4} D. Fabjan,^{2,5} E. Rasia,^{2,6} G. Murante,² L. Tornatore,² K. Dolag,^{7,8} G. L. Granato,² M. Gaspari^{9†} and A. M. Beck⁷

¹*Dipartimento di Fisica dell' Università di Trieste, Sezione di Astronomia, via Tiepolo 11, I-34131 Trieste, Italy*

²*INAF, Osservatorio Astronomico di Trieste, via Tiepolo 11, I-34131, Trieste, Italy*

³*Departamento de Astronomía y Astrofísica, Universidad de Valencia, c/Dr. Moliner, 50, E-46100 - Burjassot (Valencia), Spain*

⁴*INFN – National Institute for Nuclear Physics, Via Valerio 2, I-34127 Trieste, Italy*

⁵*Faculty of Mathematics and Physics, University of Ljubljana, Jadranska 19, 1000 Ljubljana, Slovenia*

⁶*Department of Physics, University of Michigan, 450 Church St., Ann Arbor, MI 48109, USA*

⁷*University Observatory Munich, Scheinerstr. 1, D-81679 Munich, Germany*

⁸*Max-Planck-Institut für Astrophysik, Karl-Schwarzschild Strasse 1, D-85748 Garching bei München, Germany*

⁹*Department of Astrophysical Sciences, Princeton University, Princeton, NJ 08544, USA*

Accepted 2017 February 17. Received 2017 January 27; in original form 2016 December 16

ABSTRACT

The distribution of metals in the intracluster medium (ICM) of galaxy clusters provides valuable information on their formation and evolution, on the connection with the cosmic star formation and on the effects of different gas processes. By analysing a sample of simulated galaxy clusters, we study the chemical enrichment of the ICM, its evolution, and its relation with the physical processes included in the simulation and with the thermal properties of the core. These simulations, consisting of re-simulations of 29 Lagrangian regions performed with an upgraded version of the smoothed particle hydrodynamics (SPH) *GADGET-3* code, have been run including two different sets of baryonic physics: one accounts for radiative cooling, star formation, metal enrichment and supernova (SN) feedback, and the other one further includes the effects of feedback from active galactic nuclei (AGN). In agreement with observations, we find an anti-correlation between entropy and metallicity in cluster cores, and similar radial distributions of heavy-element abundances and abundance ratios out to large cluster-centric distances ($\sim R_{180}$). In the outskirts, namely outside of $\sim 0.2 R_{180}$, we find a remarkably homogeneous metallicity distribution, with almost flat profiles of the elements produced by either SNIa or SNII. We investigated the origin of this phenomenon and discovered that it is due to the widespread displacement of metal-rich gas by early ($z > 2-3$) AGN powerful bursts, acting on small high-redshift haloes. Our results also indicate that the intrinsic metallicity of the hot gas for this sample is on average consistent with no evolution between $z = 2$ and $z = 0$, across the entire radial range.

Key words: methods: numerical – galaxies: clusters: general – galaxies: clusters: intracluster medium.

1 INTRODUCTION

In the hierarchical model of structure formation, galaxy clusters, the youngest and largest cosmic structures to form, emerge from the gravitational collapse of large overdense regions in the matter distribution. Although most part of the cluster mass (typically, 10^{14} – $10^{15} M_{\odot}$) is in the form of dark matter (~ 85 per cent), whose dynamics dominates the cluster formation, there is also a contribu-

tion from stars in galaxies (~ 5 per cent) and from a hot ($T \sim 10^7$ – 10^8 K) and diffuse plasma, the intracluster medium (ICM; ~ 10 – 15 per cent), which can be observed through its X-ray emission (see Kravtsov & Borgani 2012; Planelles, Schleicher & Bykov 2016a, for reviews). Given their large masses, clusters are characterized by very deep gravitational potential wells which allow us to study in detail all the baryonic processes affecting both the stellar component and the hot ICM simultaneously.

X-ray spectral observations of galaxy clusters (see Böhringer & Werner 2010, for a review) provide important information on the ICM temperature and density, and on the abundance of different metals (chemical elements heavier than helium). These metals are

★ E-mail: biffi@oats.inaf.it

† Einstein, Spitzer Fellow.

mainly released during the life phases of low- and intermediate-mass stars within galaxies and by supernova (SN) explosions. In particular, whereas core-collapse or Type II supernovae (SNII) are mainly responsible for the production of light metals (such as O, Ne, Mg or Si – but contribute also to Fe enrichment), Type Ia supernovae (SNIa) produce large amounts of heavier metals (principally, Fe and Ni). Intermediate-mass elements, such as, Si, S, Ar or Ca, are produced by both SNe types in similar proportions, whereas lighter elements (C, N) are contributed by low- and intermediate-mass stars during their Asymptotic Giant Branch (AGB) phase. In addition to the different metal production, SNII and SNIa also show different time-scales in releasing the metals. In fact, while the former result from high-mass stars, whose lives are short and trace therefore recent star formation episodes, the latter result from long-lived low-mass stars and can thus be delayed by billions of years from the time of star formation, contributing to the late enrichment. Therefore, observations of the relative abundance ratios of different elements, and their spatial distributions within the cluster volume, provide valuable information on the number and distribution of each SN type and on their metal production efficiency throughout the cluster evolution. Moreover, the fact that the ICM is metal-rich throughout the cluster volume (and not only in the centre of star forming galaxies) suggests that there should be an interplay between a number of astrophysical and dynamical processes, such as galactic winds, active galactic nuclei (AGN) feedback or ram-pressure stripping, which contribute to mix and redistribute the metal content of the ICM (e.g. Churazov et al. 2001; Rebusco et al. 2005, 2006; Simionescu et al. 2008, 2009; Gaspari et al. 2011a,b; Kirkpatrick & McNamara 2015).

The first observations with enough sensitivity to study the ICM metal content were provided by the X-ray satellites *ASCA* and *BeppoSAX*. Early *ASCA* observations confirmed an average Fe enrichment in the ICM of around $\sim 1/3$ of the solar abundance and provided, for the first time, abundance measurements for other elements (e.g. Mushotzky et al. 1996; Finoguenov, David & Ponman 2000). On the other hand, early observations with *BeppoSAX* of the radial distribution of the ICM Fe abundance in local massive galaxy clusters showed a significant trend: while non-cool core (NCC) clusters appear to have an almost flat iron abundance profile out to $\sim 0.4R_{180}$,¹ cool-core (CC) systems show instead a significant enhancement of the Fe abundance in their cores (De Grandi & Molendi 2001; De Grandi et al. 2004; Böhringer et al. 2004; Baldi et al. 2007).

Deeper and better resolved observations of galaxy clusters with *XMM-Newton*, *Chandra* and *SUZAKU* allowed for a more detailed analysis of the ICM metal content and its spatial distribution. In local clusters, the level of core ($r < 0.1R_{180}$) entropy anticorrelates with the central enrichment level (Leccardi, Rossetti & Molendi 2010). In addition, the analysis of the Si/Fe radial distribution reveals a nearly flat profile within the central cluster regions, suggesting a flat proportion and a similar metal contribution of SNII and SNIa (e.g. Sato et al. 2008; Sakuma et al. 2011; Matsushita et al. 2013). These X-ray observations were still limited by a relatively poor spatial resolution and, as a consequence, most of the data provided correspond to central cluster regions. More recently, observations with *SUZAKU* (e.g. Fujita et al. 2008) have provided the first ob-

servational determination of the metal abundance out to cluster outskirts (see also recent studies of the Perseus and Virgo clusters by Werner et al. 2013; Simionescu et al. 2015), confirming a relatively uniform Fe distribution throughout the cluster volume. To explain such an extended metal distribution, an early ($z > 2$) ICM enrichment is required.

A number of studies have also addressed the z -evolution of the ICM metal abundance, suggesting, however, contradictory trends (e.g. Balestra et al. 2007; Maughan et al. 2008; Andreon 2012; Baldi et al. 2012; Ettori et al. 2015; McDonald et al. 2016). Recently, cluster observations by McDonald et al. (2016), out to $z \sim 1.5$, report a weak z -evolution of the central metallicity in CC clusters, although this correlation seems to be less strong than the one reported by Ettori et al. (2015). Instead, when the core is excised, either works do not find a significant difference between CC and NCC clusters and both populations seem to show a non-evolving metal abundance in their outer regions (see Molendi et al. 2016, for a critical analysis of the difficulties in assessing observationally the ICM metal content).

Within this context, cosmological hydrodynamical simulations of galaxy clusters are extremely useful to shed some light on the complex processes affecting the ICM metal distribution, its z -evolution, its connection with the metal production by different SN types, its relation with existing dynamical and feedback processes and the possible biases on the metallicity measures (e.g. Tornatore et al. 2004, 2007; Cora et al. 2008; Fabjan et al. 2008, 2010; Rasia et al. 2008; McCarthy et al. 2010; Planelles et al. 2014; Martizzi et al. 2016). Any hydrodynamical simulation that tries to describe, consistently with the cosmic evolution, the production of heavy elements must couple complicated models of chemical enrichment with a number of subgrid physical processes, such as star formation, SN feedback, galactic winds or AGN feedback. These chemical evolution models (characterized by a number of elements, such as the SNe explosion rates and lifetime functions, the stellar yields or the initial mass function) are crucial to obtain a global picture of the cosmic enrichment. Indeed, despite the inevitable uncertainties associated with these models, cosmological hydrodynamical simulations, including different chemical enrichment schemes, have confirmed many of the observations of the local metal content in galaxy clusters (see Borgani et al. 2008, for a review).

In this paper, we take advantage of the simulated sample of galaxy clusters recently presented by Rasia et al. (2015) that include the effects of radiative cooling, star formation, chemical enrichment and AGN feedback. These simulations, for the first time, reproduce the observed ratio of CC and NCC clusters and are in good agreement with observations, in terms of iron abundance and entropy profiles. Starting from this result, we perform, here, a detailed analysis of the ICM metal distribution. In particular, the abundances, spatial distributions and ratios of different elements, such as Fe, Si and O, will be analysed as a function of the different physics included in the simulations, the cool-core-ness of the systems and the z -evolution. The production of metals by different sources tracked in the simulations, namely, SNIa, SNII and AGB stars, will be also discussed.

The organization of the paper is as follows. A brief description of our simulations, together with the main properties of the sample of clusters to be analysed, is introduced in Section 2. Results on the chemical properties of our set of simulated galaxy clusters at $z = 0$ are shown in Section 3, whereas the z -evolution of the ICM chemical enrichment is analysed in Section 4. In Section 5 we discuss the effects of AGN feedback on the distribution of heavy elements in

¹ R_{180} is defined as the radius of the sphere enclosing the volume of the cluster whose mean density equals 180 times the critical density of the Universe. In a similar way, we will also define R_{200} and R_{500} , used in the following.

the ICM, and in Section 6 we present the different contributions to the ICM metal content by three different enrichment sources. Finally, in Section 7 we discuss and summarize our main findings.

2 NUMERICAL SIMULATIONS

The numerical simulations analysed in this paper have been already presented in a number of recent works (Rasia et al. 2015; Biffi et al. 2016; Planelles et al. 2016b; Truong et al. 2016; Villaescusa-Navarro et al. 2016). Therefore, here we only detail the most relevant features for the current study. For further numerical or technical information on this set of simulations, we refer the reader to these papers.

Our set of simulations consists in 29 zoomed-in Lagrangian regions simulated with an upgraded version of the GADGET-3 code (Springel 2005). These regions, selected from a parent DM-only simulation, were extracted around 24 dark matter haloes with $M_{200} > 8 \times 10^{14} h^{-1} M_{\odot}$ and five smaller ones with $M_{200} = [1 - 4] \times 10^{14} h^{-1} M_{\odot}$ (see Bonafede et al. 2011, for more details). Each low-resolution region was then re-simulated to achieve better resolution and include the contribution from baryons. The simulations have been run with these cosmological parameters: $\Omega_m = 0.24$, $\Omega_b = 0.04$, $n_s = 0.96$, $\sigma_8 = 0.8$ and $H_0 = 72 \text{ km s}^{-1} \text{ Mpc}^{-1}$.

The mass resolution for the DM and gas particles is $m_{\text{DM}} = 8.47 \times 10^8 h^{-1} M_{\odot}$ and $m_{\text{gas}} = 1.53 \times 10^8 h^{-1} M_{\odot}$, respectively. For the gravitational force, a Plummer-equivalent softening length of $\epsilon = 3.75 h^{-1} \text{ kpc}$ is used for DM and gas particles, whereas $\epsilon = 2 h^{-1} \text{ kpc}$ for black hole and star particles. The DM softening length is kept fixed in comoving coordinates for $z > 2$ and in physical coordinates at lower redshift. For the other components, the softening lengths are always determined in comoving coordinates.

As for the hydrodynamical scheme, the improved smoothed particle hydrodynamics (SPH) formulation, described by Beck et al. (2016), was implemented. This new SPH model, which includes artificial thermal diffusion and higher-order interpolation kernel, improves the standard SPH performance in its capability of treating discontinuities and following the development of gas-dynamical instabilities.

Our set of simulations includes different treatments of baryonic physics. In particular, in the following we will analyse two of them:

(i) CSF. These simulations include radiative cooling, star formation, SN feedback and metal enrichment, as introduced in Planelles et al. (2014). Namely, star formation and stellar feedback are implemented according to the original model by Springel & Hernquist (2003), the heating/cooling from cosmic microwave background (CMB) and from a UV/X-ray time-dependent uniform ionizing background are included as in Haardt & Madau (2001), and the rates of radiative cooling follow the prescription by Wiersma, Schaye & Smith (2009).

(ii) AGN. These runs include the same physical processes as in the CSF case, but account as well for AGN feedback. Our model for SMBH accretion and AGN feedback was presented in Steinborn et al. (2015).

2.1 The model for chemical enrichment

Stellar evolution and metal enrichment are included following the original formulation by Tornatore et al. (2007).

Our model of star formation is an updated version of the original implementation by Springel & Hernquist (2003). In particular, gas particles with a density above 0.1 cm^{-3} and a temperature below

$2.5 \times 10^5 \text{ K}$ are classified as multiphase, with a cold and a hot-phase coexisting in pressure equilibrium. The cold phase represents the reservoir for star formation.

The production of heavy elements considers the contributions from SNIa, SNII and AGB stars. Whereas all three types of stars contribute to the chemical enrichment, only SNIa and SNII provide as well thermal feedback. In addition, as described in Springel & Hernquist (2003), kinetic feedback from SNII is implemented as galactic outflows with a wind velocity of 350 km s^{-1} . The distribution of initial masses for the population of stars is provided by the initial mass function of Chabrier (2003). We assume the mass-dependent lifetimes of Padovani & Matteucci (1993) to account for the different time-scales of stars of different masses.

To estimate the abundance of the different metal species produced during the evolution of a stellar particle, we consider different sets of stellar yields. In particular, we have adopted the yields provided by Thielemann et al. (2007) for SNIa stars and those by Karakas & Lattanzio (2007) for AGB stars. In the case of SNII, we use the metal-dependent yields by Woosley & Weaver (1995) combined with those by Romano et al. (2010). In our simulations, we specifically trace the production and evolution of 15 chemical elements: H, He, C, Ca, O, N, Ne, Mg, S, Si, Fe, Na, Al, Ar and Ni. Metallicity-dependent radiative cooling is included in our simulations following the approach proposed in Wiersma et al. (2009), and considering the contribution of the 15 chemical species traced by using pre-computed tables from the CLOUDY code for an optically thin gas in (photo-)ionization equilibrium.

Given the features of the chemical evolution model implemented in our simulations, it is relatively straightforward to estimate the contribution to metallicity by a particular stellar source. Therefore, at any given redshift, we can compute the amount of the mass in metals in a gas or stellar particle provided by SNIa, SNII or AGB stars. For further details on the chemical evolution model, we refer the interested reader to Tornatore et al. (2007).

Despite the large variety of physical processes treated, our simulations still present some limitations. Our chemical model, for instance, does not include any treatment of metal diffusion, although the code accounts for the spreading of metals from star particles to the surrounding gas particles, by using the same kernel of the SPH scheme. This is mainly done in order to avoid a noisy estimation of metal-dependent cooling rates, and thus heavy elements can be spatially distributed only via dynamical processes involving the metal-rich gas. Also, another important process that is not yet accounted for in our simulations is the metal depletion due to the formation of dust grains. Since a possibly large fraction of heavy elements (especially C, O, S, Fe, Mg, Si) are likely to be locked into dust, solid particles, this could also affect the distribution of gas-phase metallicity. For a comprehensive study of the enrichment level in clusters, in which a full picture of the heavy-elements cycle among the cluster baryonic components (stars, multi-phase ICM and dust) can be drawn, these effects should be ultimately taken into account.

2.2 The set of simulated clusters

For the purpose of the present analysis, we concentrate on the 29 main haloes residing in each of the re-simulated Lagrangian regions. The sample consists of 29 clusters with masses $6 \times 10^{13} h^{-1} M_{\odot} \leq M_{500} \leq 2 \times 10^{15} h^{-1} M_{\odot}$ at $z = 0$ (e.g. Planelles et al. 2014). Their centre is found by applying a Friends-of-Friends (FoF) analysis to identify the position of the particle with the minimum of

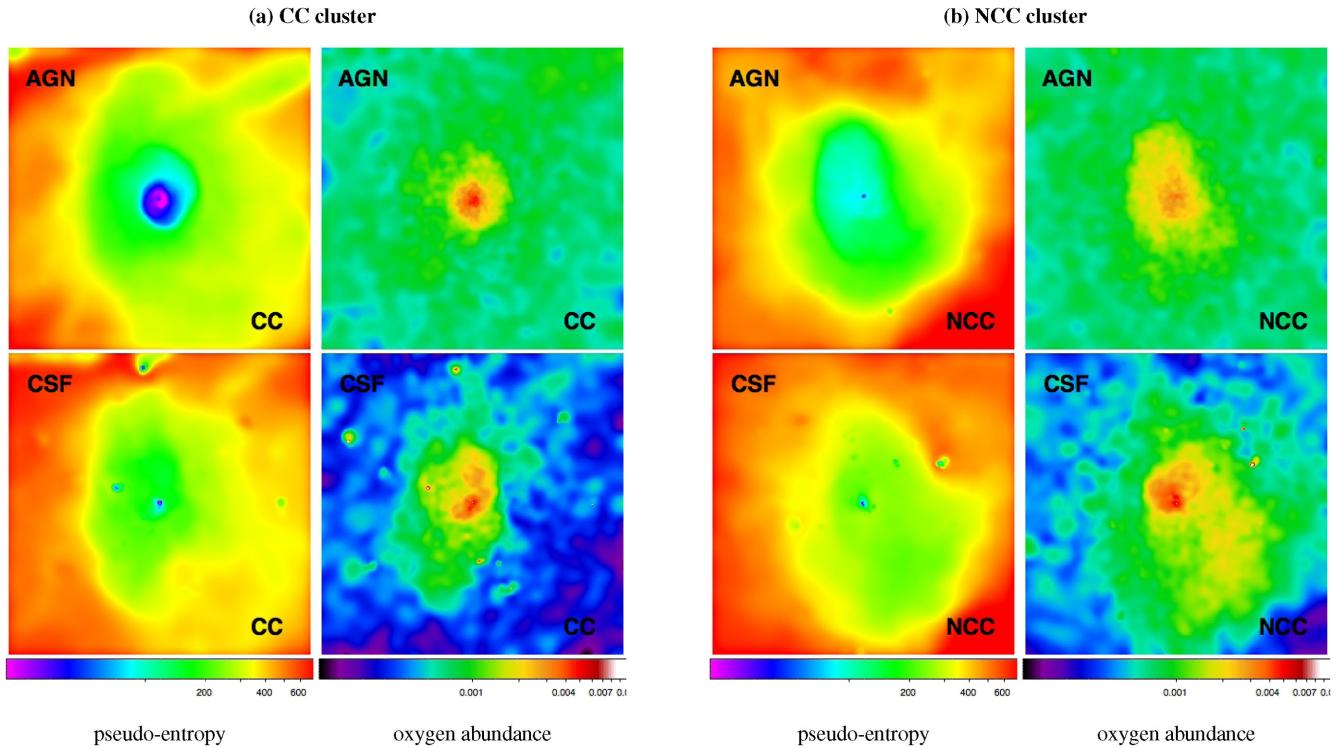


Figure 1. Projected maps of pseudo-entropy (left) and oxygen abundance (right) for a CC (a) and a NCC (b) cluster in the sample, at $z = 0$. For each cluster we show both the result from the AGN run (top panels) and from the CSF one (bottom panels). The pseudo-entropy maps are derived from the maps of spectroscopic-like temperature and X-ray soft band ([0.5–2] keV) emissivity combined as $\mathcal{M}_{\text{TSL}}/\mathcal{M}_{\text{SXR}}^{1/3}$. The oxygen abundance is reported as mass fraction with respect to hydrogen. Each map is centred on the position of the minimum of the cluster potential well, and comprises a region of 2 Mpc per side and 5 Mpc of integration along the line of sight.

the gravitational potential within the FoF group. Given this, we determine the cluster virial radius R_{vir} by adopting a spherical collapse algorithm, based on this centre. R_{vir} is defined as the radius encompassing an average overdensity, Δ_{vir} , which is equal to the overdensity predicted by the spherical collapse model (e.g. Bryan & Norman 1998), in units of the critical density of the Universe $\rho_c(z) = 3H(z)/(8\pi G)$. In addition to R_{vir} , we will also make use of radii defined for $\Delta = 500, 200, 180$,² in order to either ease the comparison to particular observational data sets or to investigate the predicted properties of the simulated clusters within interesting regions.

As presented in Rasia et al. (2015), our AGN simulations reproduce the diversity of core thermodynamical properties observed in real clusters, with entropy and metallicity profiles that resemble quite well the differences between observed CC and NCC populations. These two classes were defined on the basis of observational criteria. In particular, we define CC cluster as a system with a central entropy³ $K_0 < 60 \text{ keV cm}^2$ and a pseudo-entropy $\sigma < 0.55$ (see Section 3.1 for the definition of the latter); we classify a cluster as a NCC when it does not satisfy both aforementioned conditions. With this classification, our sample of simulated clusters is sub-divided into 11 CC and 18 NCC. That paper demonstrates that the low isen-

tropic level reached by the CC systems is achieved thanks to the efficient AGN feedback that contrasts the radiative cooling.

The effect produced by the AGN action on the thermodynamical and metallicity properties can be appreciated in Fig. 1 where we compare two clusters classified as CC and NCC in the AGN run (Figs 1 a and b, respectively), against their CSF counterparts (lower panels). In this way, the different central thermal and chemical properties can be appreciated.

For each cluster, we show the pseudo-entropy and metallicity maps of the ICM at $z = 0$. The pseudo-entropy maps are created via simple arithmetics with the maps of the spectroscopic-like temperature, \mathcal{M}_{TSL} , and of the emissivity, \mathcal{M}_{SXR} , in the soft X-ray band ([0.5–2] keV), as $\mathcal{M}_{\text{TSL}}/\mathcal{M}_{\text{SXR}}^{1/3}$ (see e.g. Finoguenov et al. 2010). In order to visualize the ICM metallicity, we show the oxygen abundance. The maps are centred on each cluster centre and cover a volume of 2 Mpc per side, thus enclosing the projected R_{500} in both cases. The projection is done for 5 Mpc along the line of sight. The 2D maps employed are generated by using the SMAC program (Dolag et al. 2005), designed to integrate various physical and observational-like quantities (in this case, spectroscopic-like temperature, soft X-ray emissivity and oxygen abundance) through the simulation box at any given redshift.

In general, we note that both clusters appear as NCC systems in the CSF case, for what concerns the level of central (pseudo) entropy, which is significantly higher than in their AGN counterparts. In particular, the CC developed in the central region of the CC pseudo-entropy map (top-left panel in Fig. 1a) does not appear in the corresponding CSF map. Also, from the oxygen abundance maps, we notice that the difference in the level of metal enrichment

² For the clusters in our sample, $R_{500} : R_{200} : R_{180} : R_{\text{vir}}$ is on average 0.61: 0.95: 1: 1.34, at $z = 0$.

³ We adopt here the definition of ‘entropy’, K , typically used in X-ray studies of galaxy clusters, that is $K = k_B T / n_e^{2/3}$, where T is the temperature and n_e is the electron density of the gas.

in the core of the two AGN clusters, higher and more concentrated in the CC system than in the NCC one (top-right panels in the two figures), is not observed in the CSF case, where the metallicity in the core is high for both clusters (differently from observed NCC systems). The distribution of the oxygen-rich gas in the two runs, both for the CC and for the NCC cluster, also shows remarkable large-scale differences between the AGN and the CSF run. In the first case (top panels) the distribution appears to be more homogeneous, with a generally higher value of Z_O out to ~ 1 Mpc from the cluster centre. Instead, the CSF clusters present a more clumpy distribution of the oxygen, with high-metallicity small-scale substructures, well outside the central $\sim (250 \text{ kpc})^2$ (enclosing approximately $\sim 0.25 R_{500}$ for both clusters). From the visual comparison of the AGN and the CSF oxygen maps we can already infer that the gradient of the ICM metallicity from the cluster centre to the outskirts is steeper in the CSF clusters.

3 METAL ENRICHMENT OF THE ICM

Here, we present the chemical properties of the 29 simulated galaxy clusters, at redshift $z = 0$. These results are also compared to available observations of clusters in the local Universe.

For the purpose of a fair comparison to the X-ray observational data, we will consider projected quantities weighted by the emissivity of the gas. These will include a large volume of the cluster due to the integration along the line of sight.

The intrinsic metal content of the ICM will instead be evaluated by computing the three-dimensional mass-weighted (MW) values, for both global quantities and radial profiles.

Throughout the paper, the reference solar values are assumed according to the abundance pattern reported by Anders & Grevesse (1989).⁴ Observational results are therefore rescaled to these, when different.

3.1 The entropy–metallicity relation

As a first test on the connection between thermodynamical and chemical properties of the simulated clusters in the AGN run, we explore the relation between the pseudo-entropy ratio σ and the central metallicity, at $z = 0$. This is shown in Fig. 2.

The pseudo-entropy ratio is defined as $\sigma = (T_{\text{IN}}/T_{\text{OUT}}) \cdot (\text{EM}_{\text{IN}}/\text{EM}_{\text{OUT}})^{-1/3}$, with the spectroscopic-like temperature (T) and emission measure (EM) computed within the projected ‘IN’ and ‘OUT’ regions, corresponding to $r < 0.05 R_{180}$ and $0.05 R_{180} < r < 0.2 R_{180}$, respectively (e.g. Leccardi et al. 2010; Rossetti et al. 2011). The metallicity is computed as the emission-weighted (EW) iron abundance within the projected ‘IN’ region.

In Fig. 2, we compare the simulation predictions to observational findings by Leccardi et al. (2010), shown in green. To this scope, the projected values of both metallicity and pseudo-entropy are computed in cylindrical regions of $2 R_{\text{vir}}$ -length along the line of sight. In general, the differences in normalization can be related to several factors. For instance, the yields considered in the numerical modelling, the assumed initial mass function within the simulations, as well as the lack of a treatment of proper metal diffusion and dust depletion, can affect the level of chemical enrichment of the ICM.

⁴ Specifically, the solar abundance values we use are: 4.68×10^{-5} for Fe, 3.55×10^{-5} for Si and 8.51×10^{-4} for O (number fractions, relative to hydrogen).

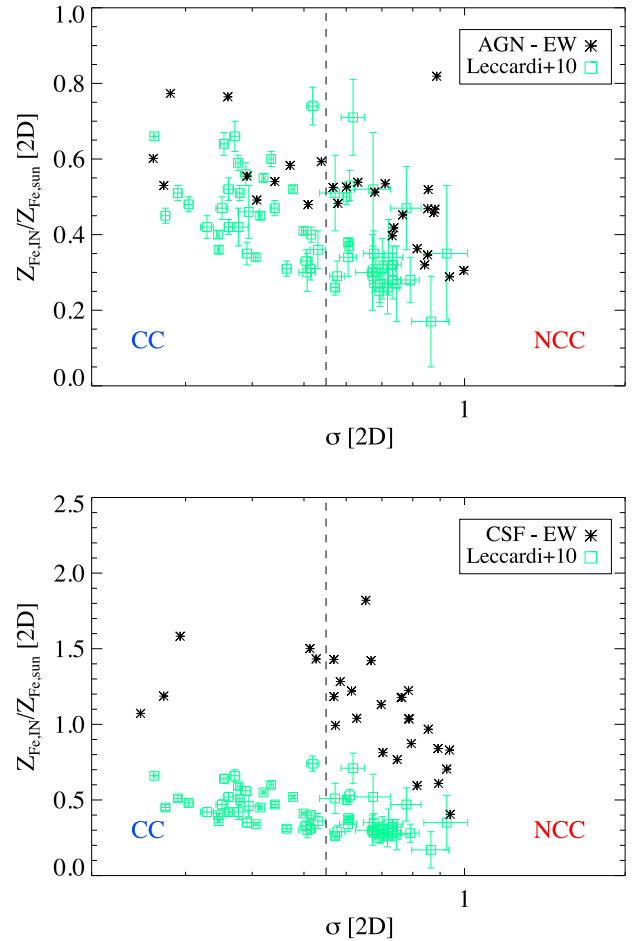


Figure 2. Relation between EW metallicity and pseudo-entropy ratio at $z = 0$, for our sample of clusters (black asterisks). The upper panel shows projected (2D) simulation data for the AGN run, whereas the lower panel displays the same quantities for the CSF set. In both cases, we show observational data from Leccardi et al. (2010), for comparison (green squares with error bars). The vertical dashed line at $\sigma = 0.55$ marks the threshold separating between CC and NCC [originally applied to 3D values of σ in Rasia et al. (2015)]. Notice the different y-axis range.

We recover the observed anti-correlation between $Z_{\text{Fe, IN}}$ and σ , namely the lower the pseudo-entropy, the stronger the metallicity peak. Specifically, the best fit⁵ to the anti-correlation for the simulated data provides a normalization of $A_{\text{sim}} = 0.76 \pm 0.05$ and a slope of $\beta_{\text{sim}} = -0.41 \pm 0.07$, respectively. Compared to the observational data by Leccardi et al. (2010), we therefore find an ~ 15 per cent higher, albeit consistent at 1σ , normalization (with respect to $A_{\text{obs}} = 0.66 \pm 0.05$, for the observed relation). Concerning the slope, our result is instead fully consistent with the observed value of $\beta_{\text{obs}} = -0.47 \pm 0.10$.⁶ The good agreement in slope confirms that our AGN simulations are capable of obtaining metal-rich gas that also tends to be the low-entropy gas. The intrinsic scatter is relatively similar, that is ~ 8 per cent for the simulations and

⁵ We follow a Bayesian approach to linear regression, and perform the fit by using the IDL macro `linmix_err.pro` by B.C. Kelly (Kelly 2007).

⁶ We fit both simulated and observed data by using the observational errors for the latter, and considering a constant error value, equal to 0.01, in both variables in the former case.

Table 1. Median values of pseudo-entropy and metallicity for the AGN and CSF simulated samples at $z = 0$. The distributions used for the projected values (columns 3 and 4) are the EW estimates shown in Fig. 2. For the three-dimensional case, the values reported are MW instead, and also the results for the ‘OUT’ region are reported (columns 5–7), as in the top panel of Fig. 5.

		2D [EW]		σ	3D [MW]	
		σ	$Z_{\text{Fe, IN}}/Z_{\text{Fe, } \odot}$		$Z_{\text{Fe, IN}}/Z_{\text{Fe, } \odot}$	$Z_{\text{Fe, OUT}}/Z_{\text{Fe, } \odot}$
AGN	All	0.68	0.51	0.81	0.47	0.28
	CC	0.41	0.58	0.42	0.50	0.28
	NCC	0.82	0.47	1.06	0.43	0.28
CSF	All	0.70	1.07	0.86	0.99	0.37

~ 10 per cent in the observations. To obtain these results we exclude the data point corresponding to the outlier in the top-right region of the plot. Through a deeper investigation, this cluster appears to be a very small mass system with a significant substructure interacting with the main halo. During its redshift evolution, this kind of interactions has affected the build-up of a CC without removing, however, the highly enriched gas from its central regions.

For comparison, we show in the lower panel of Fig. 2 the entropy–metallicity relation, at $z = 0$, for the CSF sample of simulated clusters. (Notice that the maximum value shown in the y-axis has been changed to accommodate the CSF results.) In this case, the slope is found to be excessively steep in comparison to the one observed. From the distribution of the data points we note that there is a significant enhancement of the median EW Fe abundance in the core region, from $Z_{\text{Fe, IN}} = 0.51$ for the AGN sample to $Z_{\text{Fe, IN}} = 1.07$ for the CSF, as well as an extension of the range covered especially towards high-metallicity values. Additionally, we find an overall shift of the majority of the clusters towards higher values of the pseudo-entropy σ . Median values of the distributions shown in Fig. 2 are reported in Table 1. In the CSF run, the lack of an efficient form of feedback, such as from AGN sources, prevents the formation of realistic CC clusters and the majority of the clusters could be classified as NCC systems.⁷ Nonetheless, such systems do not resemble realistic NCC clusters either, since they present both high entropy and high metallicity in the core, whereas observed NCC systems are rather characterized by low central metallicity. Concerning the five clusters lying below the threshold used to identify CC systems, we further investigated their entropy maps and profiles and found that they showed substantial differences with respect to the typical properties of realistic CC clusters in the AGN run. For a more detailed discussion, we refer the reader to the Appendix.

3.2 ICM metallicity profiles

In order to assess the reliability of our AGN simulations with respect to the chemical properties of galaxy clusters observed in the local Universe, we also investigate the radial distribution of iron and oxygen-to-iron and silicon-to-iron abundance ratios.

In the l.h.s. panel of Fig. 3 we show in particular the projected EW profile of iron abundance, relative to the solar value, for the ICM. The black solid line refers to the median profile across the sample.

⁷ We note that the threshold $\sigma = 0.55$ used to discriminate between CC and NCC was rather applied to 3D values of σ in Rasia et al. (2015). Despite different specific values of σ , we find, nonetheless, the same classification at $z = 0$ when the projected values are used as in Fig. 2 (top).

Here, simulation predictions are compared to observational data points by Leccardi & Molendi (2008) (blue data points). We find good agreement between simulated and observed profiles, within the dispersion. Towards the centre, metallicity values in the simulations appear slightly higher and show a large scatter, with respect to observational profiles. Nevertheless, we note that the results are compatible, as the scatter around the observational data reported by Leccardi & Molendi (2008) is also high (see dashed lines reported in their fig. 2). Large scatter in the innermost regions is also found in recent high-resolution *Chandra* observations of single cluster profiles shaped by AGN feedback (e.g. Kirkpatrick & McNamara 2015).

In the r.h.s. panel of the figure, we present instead the MW, three-dimensional metallicity profiles, which quantify the intrinsic distribution of the iron-rich ICM. Colours refer to the cool-core classification (see Rasia et al. 2015) of the clusters, with CC systems marked in blue and NCC ones in red. The thick solid and dashed lines represent the median profiles of the two subsamples (CC and NCC, respectively). The 3D iron profiles show a lower Fe metallicity in the outskirts as well as a reduced scatter. This similarity of the iron content within the sample implies a homogeneous distribution of metals in the outskirts. In contrast, the larger variance seen in the EW profiles is mainly due to the presence of substructures and gas density clumps, especially at large cluster-centric distances, which more significantly affect the estimates weighted by the ICM emission (as in observations). On the other hand, the metal content of the central regions reflects the diversity of the cluster core properties. Our sample of CC clusters shows on average higher metal abundances and steeper profiles than NCC systems in the inner cluster region ($r < 0.1 R_{180}$), which is in agreement with observational findings by Ettori et al. (2015), as shown and discussed in Rasia et al. (2015).

3.2.1 Abundance ratios

In addition to studying the single chemical species, computing the relative abundance of heavy elements produced via different enrichment channels is also particularly useful in order to infer information on the chemical history of galaxy clusters.

For our AGN sample, we show in Fig. 4 the radial profiles of the abundance ratio of silicon and oxygen relative to Fe (Si/Fe in the top panels and O/Fe in the bottom panels). In the l.h.s. panels we report the projected, EW profiles computed from the simulations and observational data from *SUZAKU* for the massive galaxy clusters: AWM7 (Sato et al. 2008), Centaurus (Sakuma et al. 2011) and – only for the Si/Fe profile – Coma (Matsushita et al. 2013).

With respect to observational data, we find an overall agreement, given the large error bars on observed profiles. In particular, our findings confirm the flatness of the ICM metallicity profiles in the outer cluster regions, indicating a homogeneous distribution of the metal-enriched gas (see recent studies by Werner et al. 2013; Simionescu et al. 2015).

Interestingly, by inspecting the three-dimensional, MW abundance ratio profiles in the r.h.s. panels of Fig. 4, we confirm that the distribution of Si and O relative to Fe is intrinsically flat outside of $\sim 0.1\text{--}0.2 R_{180}$, with a very small intrinsic scatter across the sample.

This picture suggests that most of the metal enrichment of the ICM, from a combination of SNII and SNIa, occurred before the cluster formed. For this reason, it is crucial to explore the ICM enrichment history in simulations, once their reliability in describing the observational results at present time has been tested.

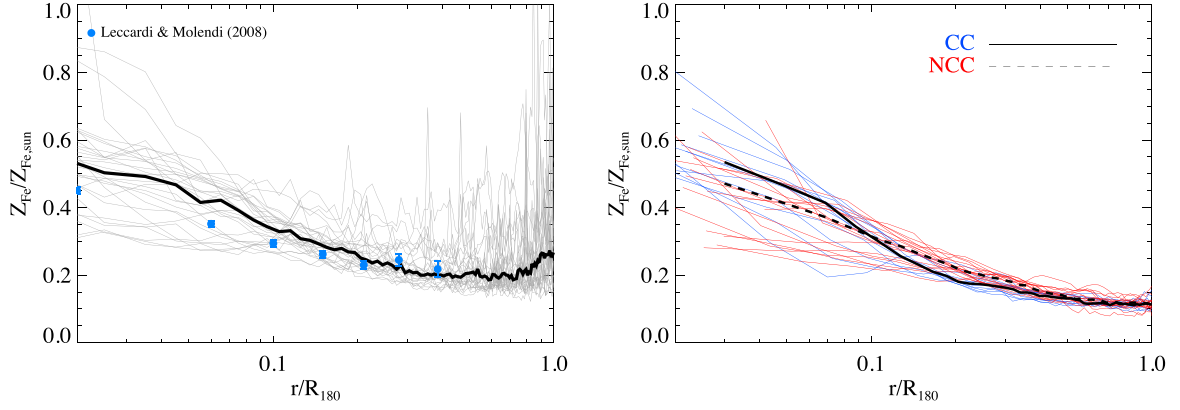


Figure 3. Radial profiles out to R_{180} of the iron abundance, relative to solar, for our samples of clusters at $z = 0$. Left: EW projected profiles compared against observational data by Leccardi & Molendi (2008) (blue circles). Marked with the solid black line we show the median profile for the 29 clusters. The integration along the line of sight covers a length of $2 R_{\text{vir}}$. Right: MW three-dimensional profiles for the CC (blue) and NCC (red) clusters separately, with the thick solid and dashed lines marking the median profiles of each subsample.

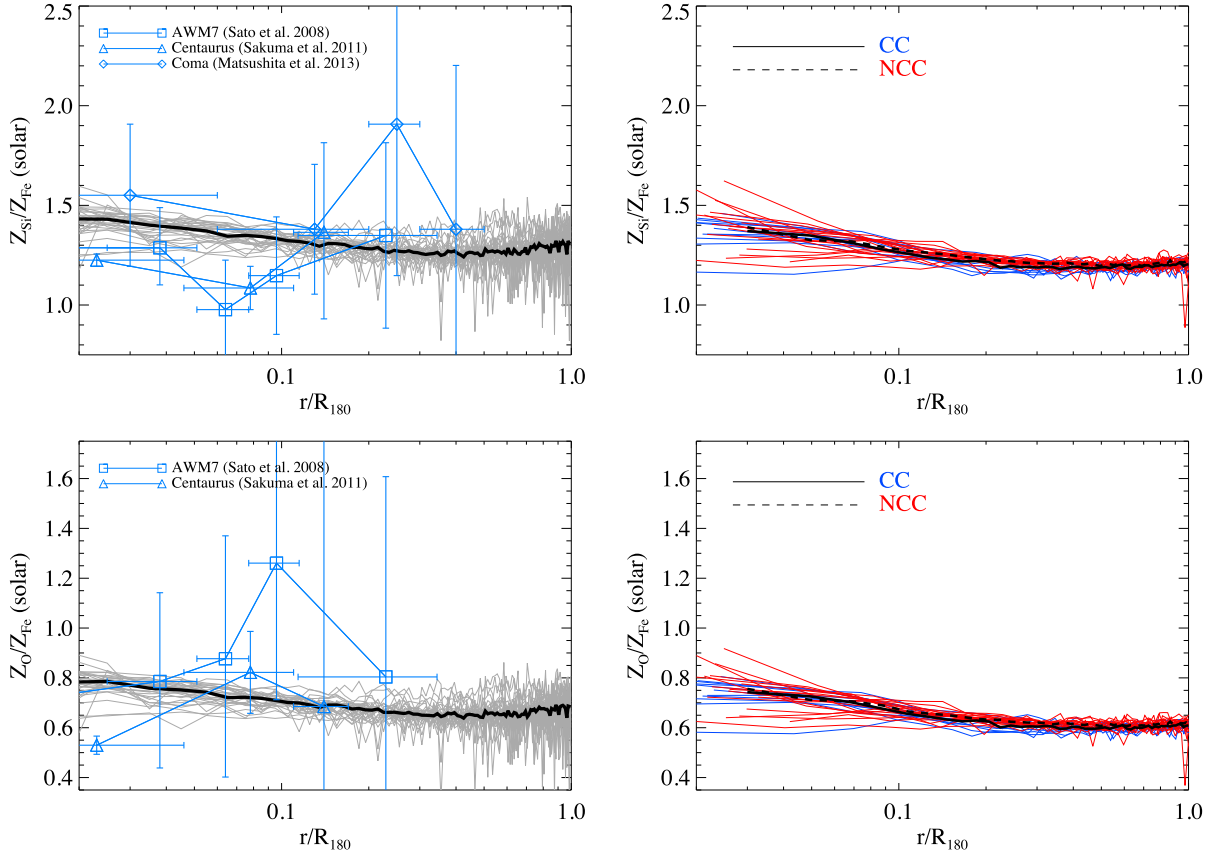


Figure 4. Radial profiles out to R_{180} of the relative abundances of Si/Fe (top panel) and O/Fe (bottom panel) for our samples of clusters at $z = 0$. Left: projected EW profiles, and median profile (thick black curve), compared to observational data (blue symbols) from *SUZAKU* observations of three massive clusters, as in the legend. Right: three-dimensional MW profiles for the CC (blue) and NCC (red) clusters in the sample.

Notice that the intrinsic abundance ratio profiles of the CC and NCC populations do not differ significantly, suggesting that the enrichment due to SNIa and SNIi has an overall similar distribution in the two cases. In fact, in our sample the behaviour of the silicon and oxygen abundances is very similar to that of iron, shown in Fig. 3 (right): typically, the CC subsample shows steeper radial

profiles that are more peaked towards the cluster centre, while the NCC systems present flatter profiles, which are higher than CC for $0.1 R_{180} < r < 0.3 R_{180}$, and reach lower metallicities in the centre. This is mirrored by the relatively flat profiles and by the lack of distinctive signatures between CC and NCC systems of the Si/Fe and O/Fe abundance ratios.

4 THE HISTORY OF THE ICM METAL ENRICHMENT

Given the relatively good agreement with projected data at $z = 0$ (Fig. 2), we use the simulated clusters to show how the relation between central entropy and metallicity evolves with time. However, in order to make a prediction on the intrinsic metal enrichment of the ICM at higher redshifts, we take advantage of the simulated data to show the MW metallicity values, and do not project along the line of sight.

In Fig. 5 we show the evolution of the intrinsic relation between MW metallicity of the innermost region of our simulated clusters and the 3D pseudo-entropy ratio. From the three panels in Fig. 5, we note that the intrinsic correlation between central metallicity $Z_{\text{Fe,IN}}$ and pseudo-entropy σ (black symbols), albeit still negative, is weaker than the one reported in Fig. 2, and essentially vanishes at $z = 2$. The mean value of the central metallicity is only slightly increasing from $\langle Z_{\text{Fe,IN}} \rangle \sim 0.43$ at $z = 2$ up to $\langle Z_{\text{Fe,IN}} \rangle \sim 0.47$ at $z = 0$. In fact, we note from the figure that the main evolutionary effects are linked to the change of the typical pseudo-entropy range with redshift, rather than to any significant change of the intrinsic enrichment level of the gas. For comparison, we also show the evolution of the relation between the pseudo-entropy σ and the metallicity in the ‘OUT’ spherical shell, which is actually the intermediate region of the clusters (i.e. $0.05 R_{180} < r < 0.2 R_{180}$). This is marked in the figure by the red symbols. In this case we find an almost flat distribution around the median value of $Z_{\text{Fe,OUT}} \sim 0.28 \pm 0.03 Z_{\text{Fe},\odot}$ at $z = 0$. This trend is confirmed also at $z = 1$ and $z = 2$, with similarly low scatter and mean values. The intrinsic level of enrichment, basically, is already established at $z \sim 1-2$, especially in the ‘OUT’ region, where the scatter across the different clusters of the sample is very low.

In Fig. 6 we show the evolution with redshift, from $z = 2$ to $z = 0$ of the median Fe abundance in the two considered regions, using the same colour scheme. The shaded areas marked in grey correspond to the dispersion around the median value at redshift $z = 0$ and show that there is very little variation with redshift from what is observed at the present time. Only at $z = 1.5$ we note an increase in the typical metallicity, both in the core and in the outer region, which is however still consistent with the $z = 0$ value, within the scatter.

Recent observational results by Ettori et al. (2015) showed a similar picture on the spatial distribution of metals in the inner and outer regions⁸ of observed CC and NCC clusters in the redshift range $0.09 < z < 1.39$. In particular, they also observe a neat decrease of the metal abundance (by a factor of up to $\sim 2-3$), moving from the inner radial bin ($< 0.15 R_{500}$) to the outer cluster regions ($> 0.4 R_{500}$), especially for CC clusters. Instead, the intermediate/outer cluster regions of both CC and NCC systems present very similar average metallicity, and low intrinsic scatter. In Ettori et al. (2015), the authors also show observational evidence of a correlation with redshift, indicating a negative evolution of the central metal abundance with z , which is not observed in the intrinsic metal enrichment of our simulated sample. Our results are also in overall good agreement with the findings by McDonald et al. (2016), where the authors investigate the evolution of the ICM metallicity in a sample of 153 galaxy clusters in the redshift range $0 < z < 1.5$, observed with the

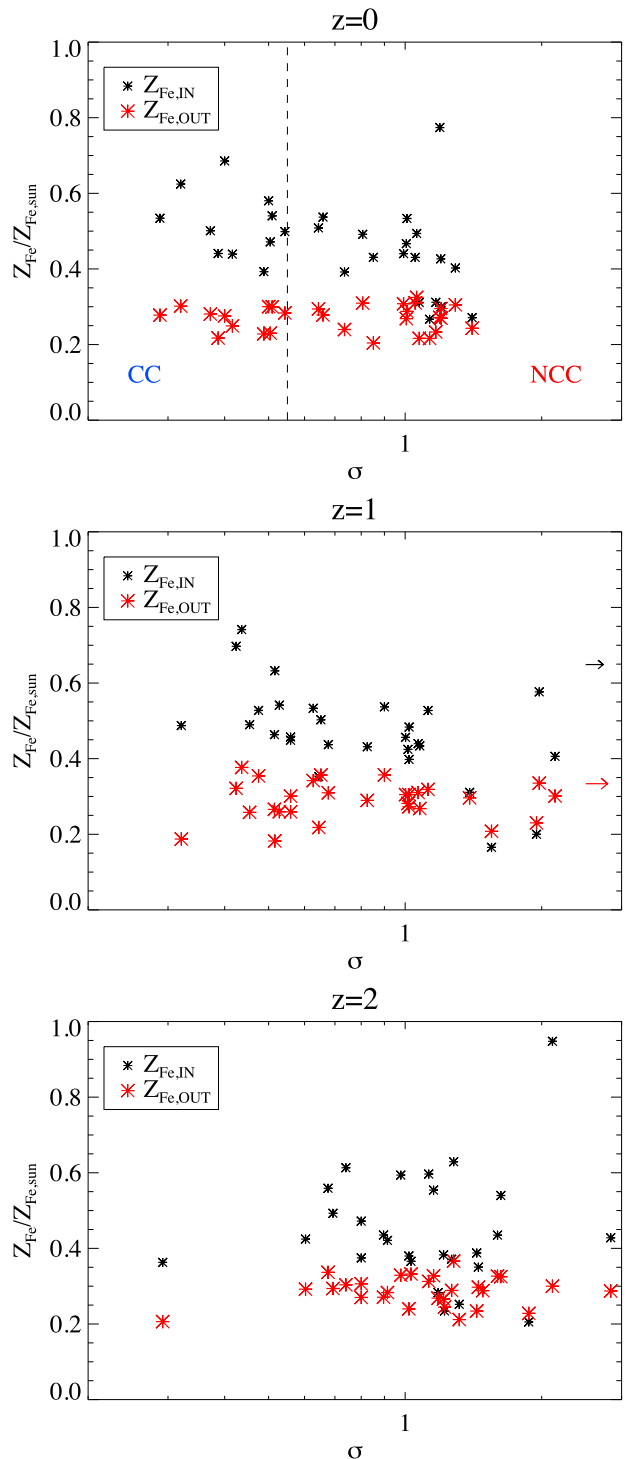


Figure 5. Relation between MW metallicity and pseudo-entropy ratio for the simulated clusters at $z = 0, 1, 2$ (from top to bottom). Values are computed within the three-dimensional ‘IN’ (black asterisks) and ‘OUT’ (red asterisks) regions, corresponding to $r < 0.05 R_{180}$ and $0.05 R_{180} < r < 0.2 R_{180}$, respectively. At $z = 0$ we report the σ -threshold used to discriminate between CC and NCC clusters (vertical dashed line). The arrows in the central panel ($z = 1$) indicate the metallicity values of a data point for which σ lies outside the plotted range.

⁸ In the analysis by Ettori et al. (2015), the authors use slightly different definitions of the radial bins used to define the inner, intermediate and outer regions: $[0-0.15] R_{500}$, $[0.15-0.4] R_{500}$ and $> 0.4 R_{500}$, respectively. We verified that this difference does not affect our conclusions.

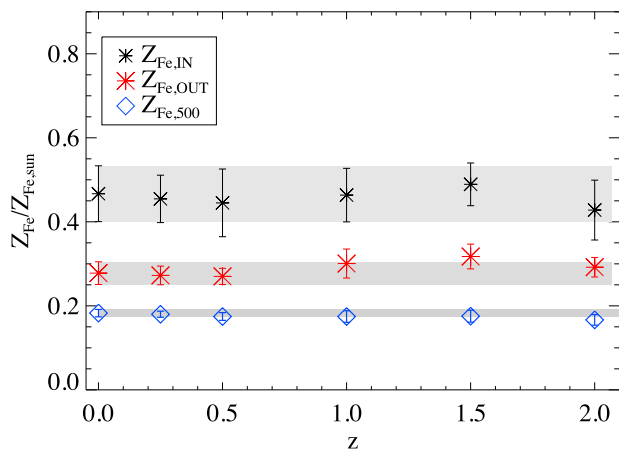


Figure 6. Evolution with redshift of the median (intrinsic, MW) iron abundance within the ‘IN’ (black asterisks) and ‘OUT’ regions (red asterisks), corresponding to $R < 0.05 R_{180}$ and $0.05 R_{180} < r < 0.2 R_{180}$, respectively. With blue diamonds we report the results for the R_{500} region. The grey shaded areas mark the dispersion around the median values at $z = 0$.

Chandra, *XMM-Newton* and *SUZAKU* telescopes. In these observations, only the CC subsample indicates a weak evolution of the central metallicity with redshift, although the correlation is found to be less strong than in Ettori et al. (2015). Instead, no significant difference is found between CC and NCC systems when the core is excised and the metal abundance is measured in the outer regions only, where no evolution is found in both cases. Also, the global metal abundance measured within R_{500} does not show any strong evidence of evolution with redshift. This is consistent with the trend observed in our simulated sample, when the global (MW and three-dimensional) iron abundance within R_{500} is concerned, as shown in Fig. 6 (blue diamonds).

We note that in both observational works, the evolution in the central metal abundance with redshift is mainly driven by the evolution observed in the core metallicity of CC clusters. In the case of our simulated sample, we are not able to perform the analysis on the separate CC and NCC subsamples, given the low statistics of CC at higher redshift. Despite this difference, the common picture outlined by both observations and simulations about the metal distribution in the intermediate-outer regions is consistent with an early-enrichment scenario, in which the bulk of the ICM metal content was produced by a mixture of SNII and SNIa, widespread and incorporated at early times ($z > 2$), even earlier than the peak of star formation and AGN activity. This is also consistent with the flat radial metallicity – and abundance ratio – profiles at large distances from the cluster centre.

4.1 Evolution of the ICM metallicity profiles

In Fig. 7, we show the evolution of the radial profiles of the Si/Fe and O/Fe abundance ratios, from $z = 2$ to $z = 0$. In order to make predictions on the intrinsic evolution of the metal enrichment of the ICM, we consider the behaviour of the median profiles computed from the whole sample of 29 clusters, where quantities are MW and profiles are three-dimensional.

From the figure, we note that the ratio of abundance profiles has similar slopes at all redshifts, although there is an obvious evolution in the normalization. The most significant difference is at $z = 2$, when the abundance ratios are typically higher than at

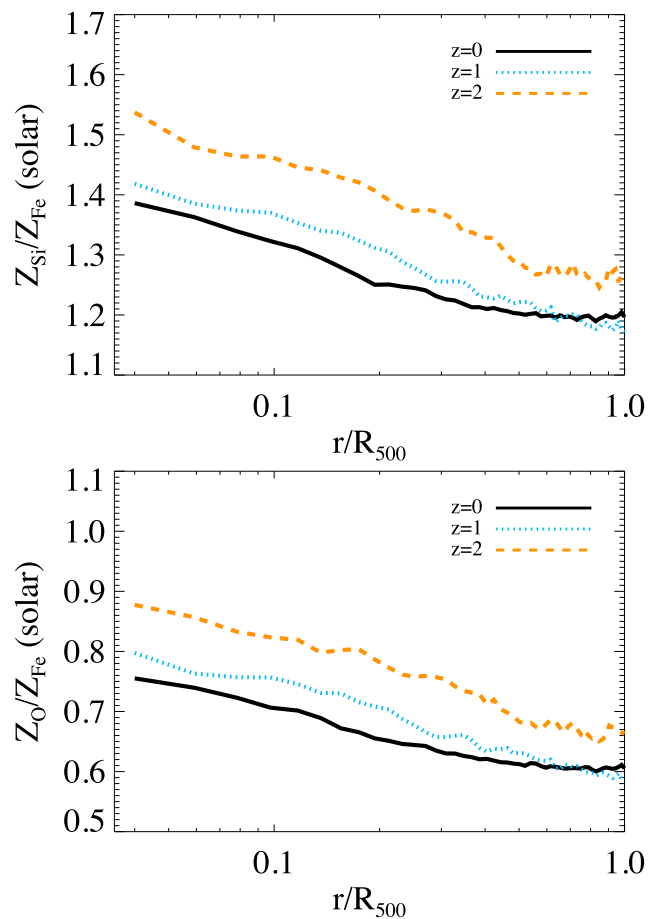


Figure 7. Evolution of the median Si/Fe (top panel) and O/Fe (bottom panel) profiles from redshift $z = 2$ to $z = 0$. The profiles are three-dimensional and the quantities MW.

lower redshifts, whereas between $z = 1$ and $z = 0$ we note a weaker evolution. With respect to $z = 0$, the $z = 2$ O/Fe abundance ratio is on average ~ 19 per cent and ~ 10 per cent higher, at $r \sim 0.15 R_{500}$ and $r \sim R_{500}$ respectively. For the Si/Fe abundance ratio, the difference is ~ 12 per cent and ~ 6 per cent at the same cluster-centric distances.

This general picture indicates that the abundance of iron relative to elements produced by SNII, such as oxygen and silicon, increases from $z = 2$ to $z = 0$. The reason for this trend is the longer time-scale that characterizes the enrichment from SNIa, associated with long-lived stars, whose contribution (and iron production) becomes therefore more and more important as time goes by.

In order to make this evolution clearer, in Fig. 8 we also report the evolution of the profiles of the three single species, singularly. From this, we note a clear difference in the normalization of the $Z(z = 2)/Z(z = 0)$ ratio, for Si, O and Fe. In the core region, the abundance of the individual species does not vary significantly from $z = 2$ to $z = 0$, in fact there is almost no evolution for the Si profile, while oxygen and iron show a 10 per cent variation at most. Nevertheless, the $z = 2$ profile of Si and O is similar or higher than the profile at $z = 0$, while the iron abundance in the same region (out to $\sim 0.15 R_{500}$) is instead lower at $z = 2$ than at $z = 0$. This opposite trend makes the difference between the O/Fe (Si/Fe) abundance ratio at $z = 2$ and that at $z = 0$ up to 20 per cent (10 per cent) in the innermost region. Overall, the systematic off-set between the Si and O curves with respect to Fe, shown in Fig. 8, is at the origin of the 10–20 per cent evolution of the O/Fe and Si/Fe abundance ratios

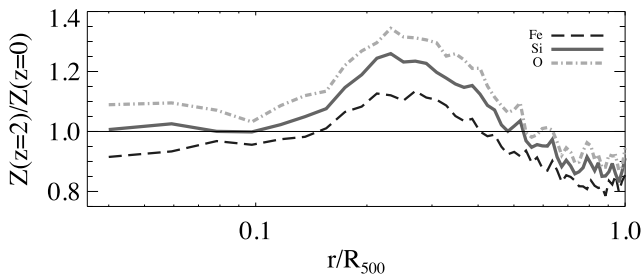


Figure 8. Comparison between the median radial profiles at $z = 2$ and $z = 0$, for Fe, Si and O, separately. As above, the profiles are three-dimensional and the quantities MW.

between redshifts 2 and 0. The curves in Fig. 8 also denote that there is a general tendency for the profiles to become from steeper at $z = 2$ to flatter at $z = 0$.

4.2 On the evolution of the baryonic total metal content

Combining the results from the previous sections, the metallicity of the hot-phase ICM at the centre (within the ‘IN’ region, i.e. $<0.05 R_{180}$) shows a very mild increase of the central Fe abundance (about 10 per cent from $z = 2$ to $z = 0$), that is however consistent with no evolution, given the scatter across the sample. The profiles shown in Fig. 8 are consistent with this picture, and with the evolution of the absolute metal content of gas and stellar component in the simulations.

In fact, this is due to the combined effect of lower-metallicity gas collapsing to more central regions during the evolution of the cluster, and of residual star formation consuming preferentially the highly enriched gas. The former contributes to maintain or even decrease the average metallicity, whereas the latter selectively removes the gas enriched by either SNII or SNIa. In the upper panel of Fig. 9, we plot the evolution from $z = 2$ to $z = 0$ of the median (MW and 3D) iron and oxygen abundances, for the star-forming gas in the ‘IN’ region. According to the effective star formation model implemented in our code (Springel & Hernquist 2003), the star-forming gas is identified with the gas particles whose density exceeds the star formation density threshold and are therefore treated as multi-phase (i.e. they contain both a hot and a cold phase in pressure equilibrium, with the latter being the reservoir for star formation – Section 2.1).⁹ Fig. 9 (upper panel) shows that the star-forming gas, from which new stars continue to form, is typically highly enriched, especially with oxygen. The difference between oxygen and iron is still related to the different enrichment channels: SNII produce a greater amount of oxygen than iron and given the short time-scale of the enrichment they likely pollute gas in the vicinity of the star-forming region. Such gas, dense and enriched, is therefore also more subject to form new stars, before moving away due to dynamical processes. This effect is less prominent for Fe, since a significant amount of Fe is produced by SNIa, whose longer time-scale allows the enrichment to happen also farther away from the star-forming regions.

Despite these effects on metallicity evolution, the total mass of metals in the gas component augments nevertheless with time, as expected, due to the metal ejection accompanying the evolution of

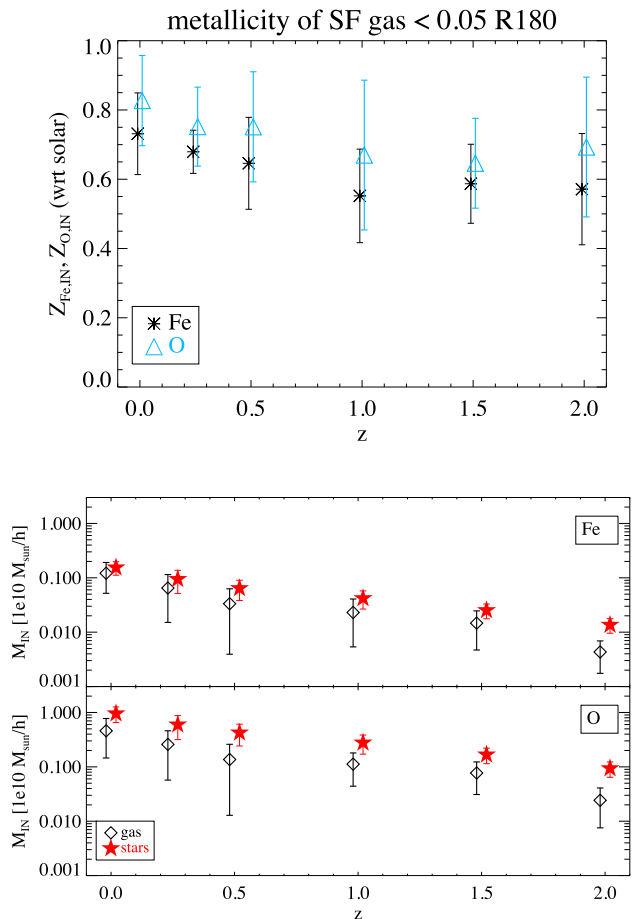


Figure 9. Upper panel: evolution of the iron (black asterisks) and oxygen (cyan triangles) abundances (with respect to solar abundances by Anders & Grevesse 1989) between $z = 2$ and $z = 0$, for the star-forming gas residing at each redshift within $0.05 R_{180}$. Lower panel: redshift evolution of the total iron (upper inset) and oxygen (lower inset) mass contained, respectively, in the gas (hot and SF; black diamonds) and stellar (red filled stars) components, residing within $0.05 R_{180}$. In both panels, symbols indicate the median value and the scatter across the 29 clusters, at each redshift z .

the stellar component. As a consequence of that discussed with the upper panel of Fig. 9, also the mass of metals locked within the stellar component increases with time, due to the formation of new stars from the highly enriched gas. In fact, considering the stars and the gas within the ‘IN’ region, the amount of metals in the stars even exceeds the one in the gas, with a larger difference (by a factor of ~ 2 at $z = 0$) in the case of oxygen. This is shown in the lower panel of Fig. 9 for the gas and the stars within $0.05 R_{180}$ at each redshift, for Fe (upper inset) and O (lower inset) separately. Of the total mass of metals locked into the stars residing within the central $0.05 R_{180}$ at $z = 0$, we verified that a non-negligible fraction, about ~ 35 per cent on average, belongs to stars that formed at redshift $z < 2$.

Therefore, we remark here that the low level of evolution found for the median iron abundance of the ICM within the central ‘IN’ region strictly concerns the hot-phase gas component in the simulated clusters, which is the one responsible for the X-ray ICM emission in observed clusters. Moreover, the lack of significant evolution of the central metallicity for the whole sample is strictly related to the

⁹ Essentially, the star-forming particles are those characterized by non-zero star formation rate, $SFR > 0$.

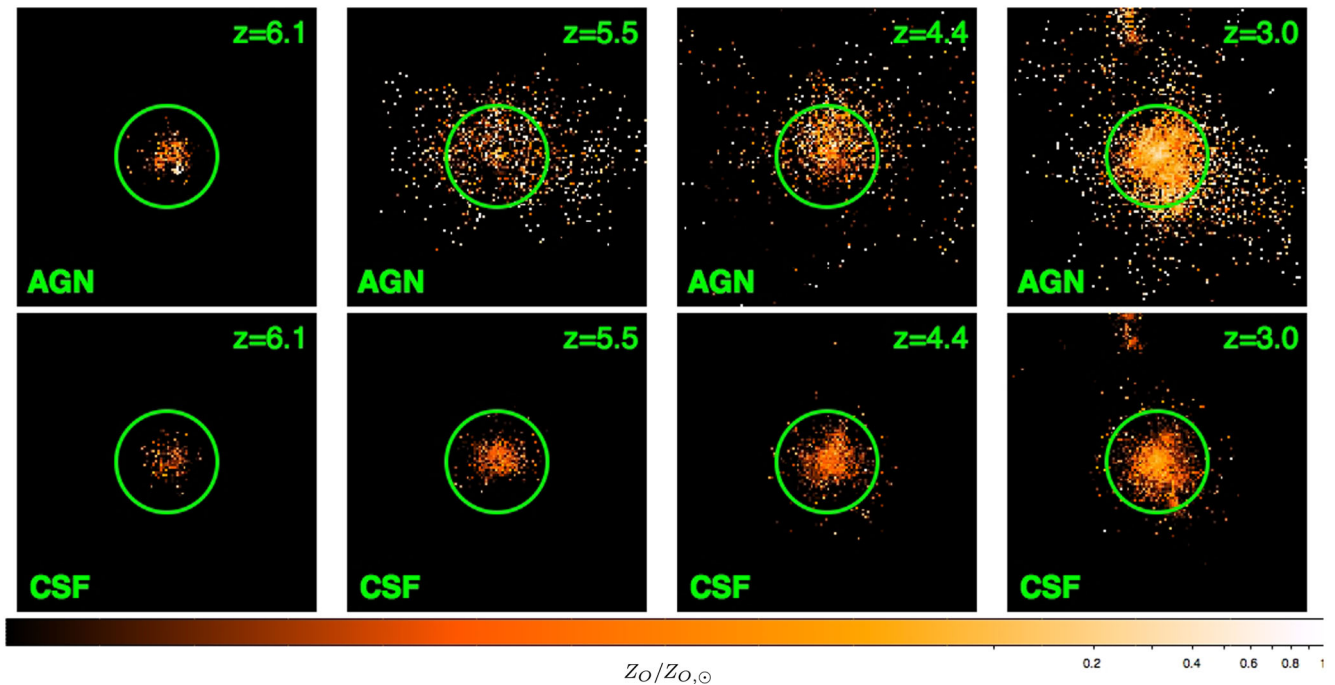


Figure 10. Oxygen maps at high redshifts for one example cluster in the runs with (top, AGN) and without (bottom, CSF) AGN feedback. From left to right, the redshifts considered are $z \sim 6.1, 5.5, 4.4, 3$. The maps cover a region of $6 R_{\text{vir}}$ per side, and 2 virial radius along the projection axis, centred on the most massive halo at each redshift. The size of the region comprised within R_{vir} is shown by the green circle.

low statistics of CC at higher redshifts, for which the evolution is observed in real clusters.

This trend observed in the core region of clusters is confirmed on larger scales. As shown in Fig. 6, similar investigations of the ‘OUT’ and R_{500} regions show in fact no evolution of the median metallicity of the hot gas with redshift. Also at larger radii, the gas in the vicinity of star-forming regions will be highly enriched with respect to the average, but will also be more likely and efficiently converted into new stars. Similarly to what happens in the core, the heavy elements in the metal-rich star-forming gas will be locked into the newly formed stars without contributing to increasing the metallicity of the hot gas. Moreover, given the accretion and infall of metal-poor gas, a certain balance is achieved also on larger scales and the average metallicity is not expected to increase significantly with time (see also Martizzi et al. 2016).

5 THE EFFECT OF THE AGN FEEDBACK

The results discussed so far indicate a relatively homogeneous distribution of metal-rich gas in the outskirts of low-redshift clusters ($z \lesssim 2$), even concerning SNII products such as oxygen. Since the distribution of metal-rich gas is very different in the case of CSF simulations, as visible from the comparison shown in Fig. 1, AGN feedback has to be crucial in shaping the metal distribution observed at the present time.

The origin of this different distribution in AGN and CSF clusters can be better understood by inspecting the spatial distribution of the metal-rich gas at higher redshifts. The oxygen abundance maps in Fig. 10 display the distribution of oxygen around the most massive halo at $z \sim 6$ in one of our Lagrangian regions, followed from $z \sim 6$ down to $z \sim 3$, for the two runs with and without AGN feedback (upper and lower panels, respectively). Each map encloses the region within $3 R_{\text{vir}}$ from the halo centre (circles mark the virial

radius of the halo at each redshift), projecting the quantities along $2 R_{\text{vir}}$ in the line of sight direction.

Already at very high redshift, $z \sim 5.5$, the difference is clearly visible: oxygen appears to be more widely spread when AGN feedback is present. The spatial spreading of oxygen-rich gas happens in the AGN run during the passage from $z \sim 6$ to $z \sim 5.5$, whereas no such spread is observed in the CSF counterpart. At $z \sim 5.5$, the gas with $Z_{\text{O}} \sim Z_{\text{O}, \odot}$ has reached distances beyond $2 R_{\text{vir}}$ from the halo centre, i.e. almost the map border, in the AGN run. On the contrary, the CSF cluster shows a much more concentrated distribution of oxygen, with the average metallicity increasing mainly in the most dense and central regions, as the system evolves.

The metal distribution can be cross-correlated with that of star-forming regions at the same redshifts, shown via the star formation rate (SFR) maps in Fig. 11. Focusing on the two left-most panels, we see that in fact the SFR in the innermost regions of the AGN system is reduced while passing from $z \sim 6$ to $z \sim 5.5$, differently than in the CSF case. At lower redshift, not only the SFR in the central regions of the CSF halo is always higher than in the AGN case, but we also notice that the distribution of oxygen continues to be typically confined to the high-SFR regions, whereas it is spread over larger areas in the AGN case. This is particularly evident at $z \sim 3$ (right-most panels), where the SFR map is spatially very similar in both runs (apart from their absolute values), while the extent of the regions characterized by oxygen-rich gas is instead clearly larger in the AGN case than in the CSF case.

From this comparison, we conclude that AGN feedback is more efficient than stellar feedback in distributing the metal-rich gas out to large cluster-centric distances, in small high-redshift haloes. Since these haloes and some of the expelled gas will be eventually accreted during the cluster mass assembly, these processes essentially favour the mixing of the pre-enriched gas that will end up in the main cluster at $z = 0$.

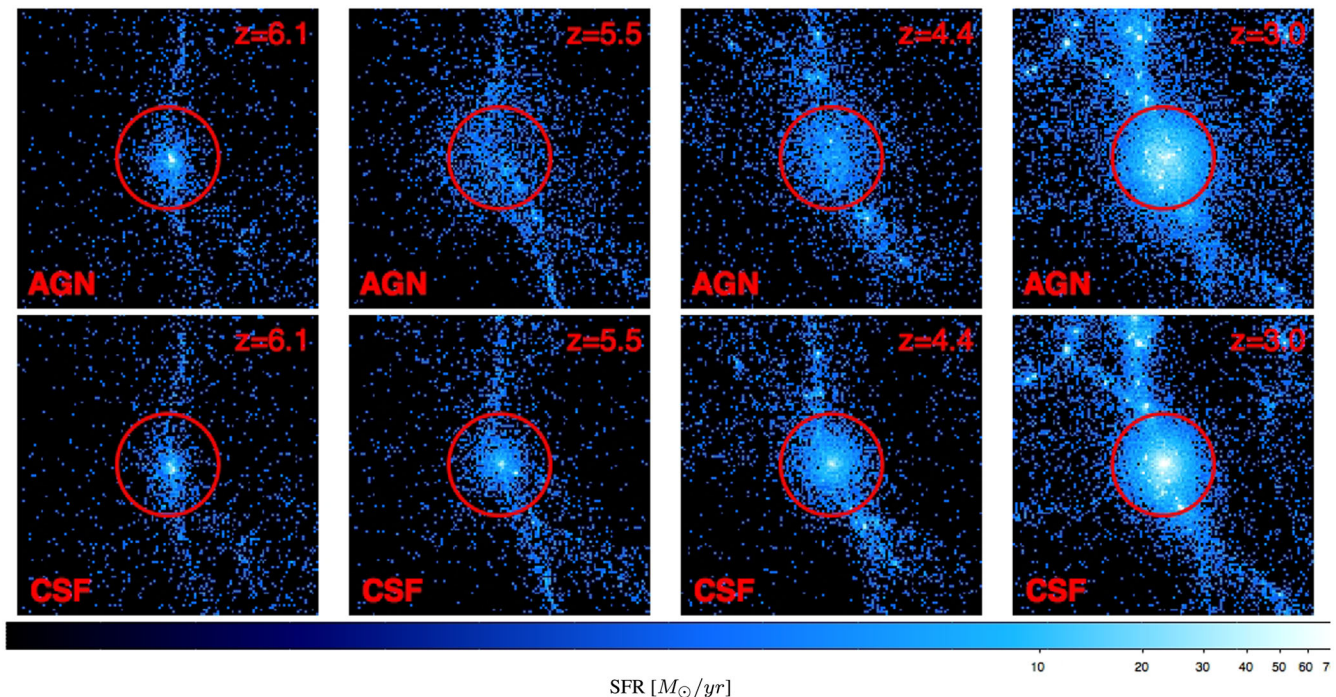


Figure 11. Similar to Fig. 10, but for the total (projected) SFR in the same region. This basically traces the presence of star-forming regions.

Therefore, AGN feedback also influences the distribution of metal-rich gas at lower redshifts ($0 \lesssim z \lesssim 2$), which is different in AGN and CSF cases. This is quantitatively investigated through the radial profiles of individual chemical species (Fe, Si and O), and abundance ratios (Si/Fe and O/Fe), at redshifts $z = 0, 1, 2$, in the following.

5.1 Metallicity profiles

In Fig. 12, we show the comparison between the iron, silicon and oxygen profiles in the AGN and CSF runs, by reporting the percentual difference between the two runs normalized to the AGN profile, versus the radial distance from the cluster centre. This emphasizes the difference between the median abundance profiles in the CSF clusters with respect to the run including AGN feedback, and their different evolution with redshift.

At $z = 0$ the CSF clusters typically have higher metal abundances than AGN ones in the central part (by a factor of ~ 2), and lower metallicities in the outskirts (by 30–50 per cent at R_{500}). The region where the excess is noticed is different for the three chemical elements, typically larger in the Fe case and smaller for Si and O, and it increases in size going from $z = 2$ to $z = 0$. This essentially indicates that in the centre of CSF clusters the metal production continues till low redshift and contributes to increase the average ICM metallicity due to the lack of an efficient feedback mechanism, able to hold back the overcooling of the gas, and quench star formation. On the contrary, the negative values of the CSF-to-AGN profile ratios in the outskirts indicate that gas metallicities at large distances from the cluster centre are higher in the AGN simulations than in the CSF run, because of the widespread distribution of metal-enriched gas following the AGN-feedback activity at high redshift ($z > 2$), as discussed with Figs 10 and 11 (see also McCarthy et al. 2011, for a study on the role of AGN feedback on the distribution of gas at high redshift).

The redshift evolution of the CSF-to-AGN ratios from $z = 2$ to $z = 0$ is also different for the three species: the iron CSF-to-AGN curve is steep at all redshifts, while it gets from shallower at $z = 2$ to steeper at $z = 0$ for Si and, especially, for O. Therefore, the difference between the slopes of the Fe profiles in the two runs must be already established at high redshift ($z = 2$), while it augments with time for both Si and O. In particular, the flatter (although still with a difference in the gradient $\gtrsim 2$) high- z CSF-to-AGN ratios for the SNII products indicate that, despite a different normalization, the metallicity gradient in the two runs is more similar than it is at $z = 0$.

Differently from iron, the oxygen CSF-to-AGN ratio at $z = 2$ is negative at all radii, further indicating that at high redshift the oxygen metallicity of AGN clusters is higher than in the CSF simulation, also in more central regions. The fact that SF should be partly suppressed in the AGN run is nevertheless still consistent with this picture. Namely, SNII products are typically released in star-forming regions, and are therefore likely to be distributed among star-forming gas particles. Especially in the CSF case where SF is not sufficiently compensated by any efficient feedback mechanism, this means that elements like silicon and oxygen have a larger probability to be rapidly locked back into newly formed stars, reducing therefore the amount of available enriched gas. Instead, given the longer time-scale associated with iron production, mainly driven by SNIa, this effect is expected to be less significant and the Fe abundance in the core of CSF clusters still exceeds the one in the AGN case (see Fabjan et al. 2010). Going to lower redshifts, this different behaviour of Fe with respect to O and Si is still visible from the ratio of CSF to AGN profiles, which is greater for iron and smaller for silicon and oxygen, in the innermost regions. Despite this, at recent times even the production of oxygen and silicon is enhanced in the CSF runs due to the higher star formation with respect to the AGN simulations, where the star formation has been quenched by the powerful feedback mechanism.

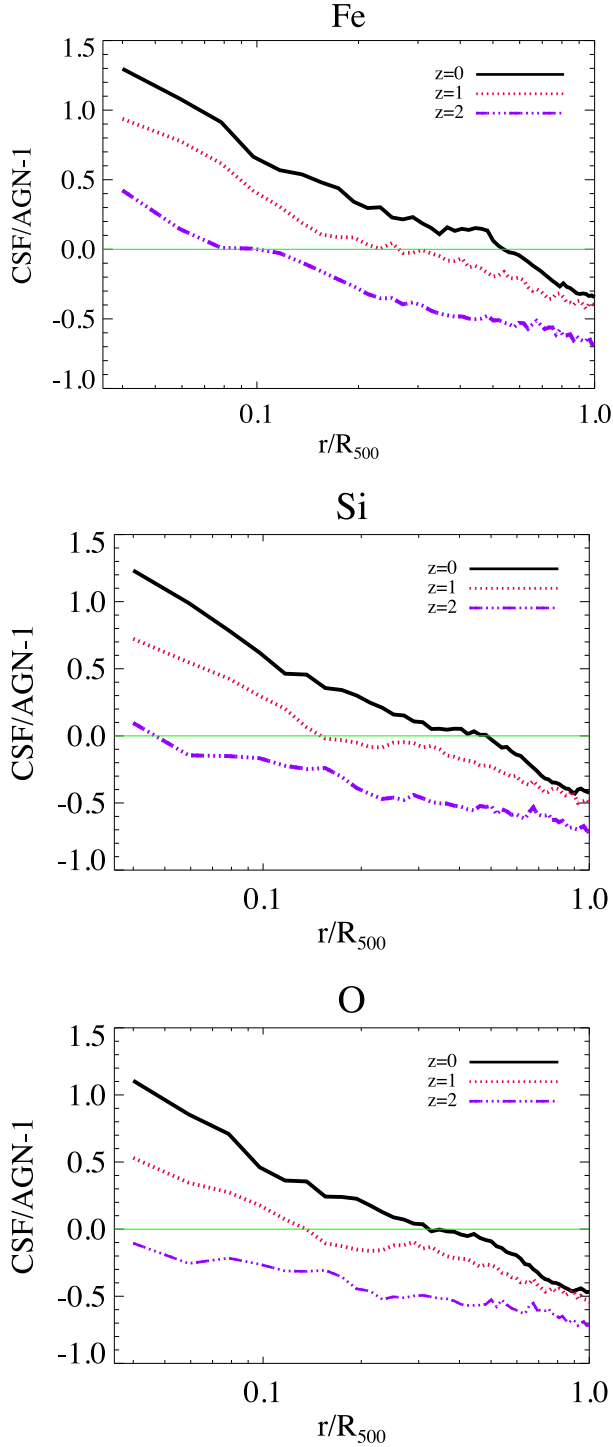


Figure 12. Comparison between the median Fe, Si and O profiles in the CSF and AGN runs at $z = 0, 1, 2$.

5.1.1 Abundance ratios

The behaviour of the three species discussed above is reflected into the CSF-to-AGN comparison of the abundance ratios and their evolution with redshift, as shown in Fig. 13.

In general, we see that the shape of the abundance ratio profiles in both AGN and CSF runs is more similar at $z = 0$ than at $z = 2$. At the present time, in fact, iron as well as silicon and oxygen presents similar differences between the two runs (see Fig. 12).

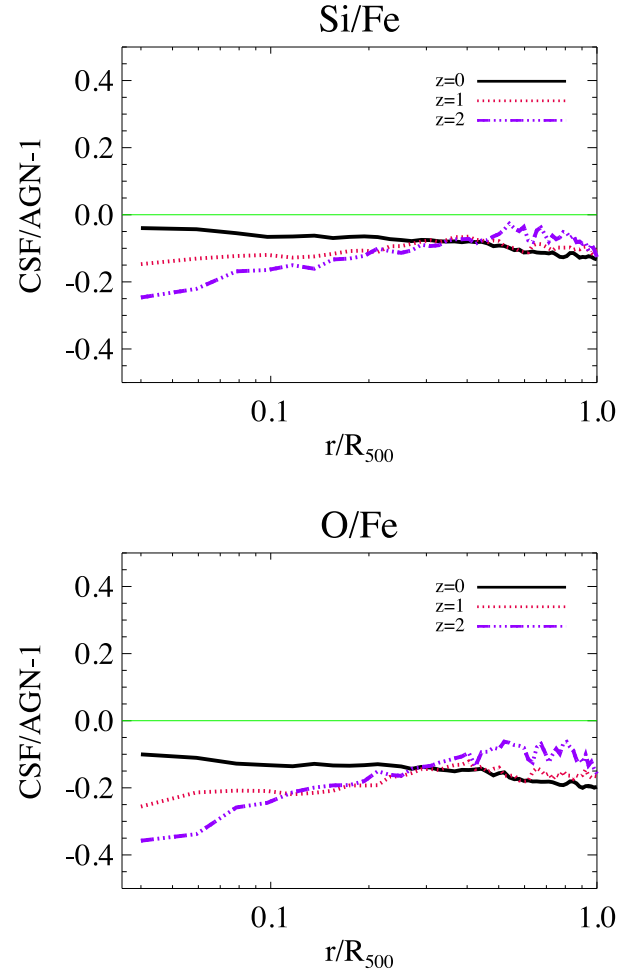


Figure 13. Comparison between the median Si/Fe and O/Fe profiles in the CSF and AGN runs at $z = 0, 1, 2$.

From Fig. 13 (upper panel), the flat and negative CSF-to-AGN curve for the Si/Fe ratio at $z = 0$ indicates that the Si/Fe profiles are almost parallel in the two runs, with an overall lower normalization in the case of the CSF clusters. The mild decrease towards the outskirts (from 5 per cent in the centre out to ~ 15 per cent at R_{500}) also suggests that the difference is not exactly constant over the radial range, but is enhanced at large distances from the cluster centre. This tells that SNII and SNIa are overall distributed similarly in both runs, even though SNII elements are less abundant, relative to Fe, in the CSF clusters (see Fig. 12).

On the contrary, at $z \sim 2$, the Si/Fe and O/Fe profiles are more similar in the outskirts, whereas the picture of the innermost region appears to be reversed. CSF clusters show a deficiency of SNII elements with respect to iron in the central region which is more severe than in the outskirts, because Fe is more abundant in the core of CSF clusters than in the AGN ones, while there is an opposite trend for Si and O (Fig. 12).

In general, we note that the difference between the CSF and the AGN abundance ratios is always within ~ 20 per cent in the region outside of $\sim 0.1\text{--}0.15 R_{500}$. Only in the central part, instead, there can be up to ~ 40 per cent difference in the O/Fe profile at $z = 2$.

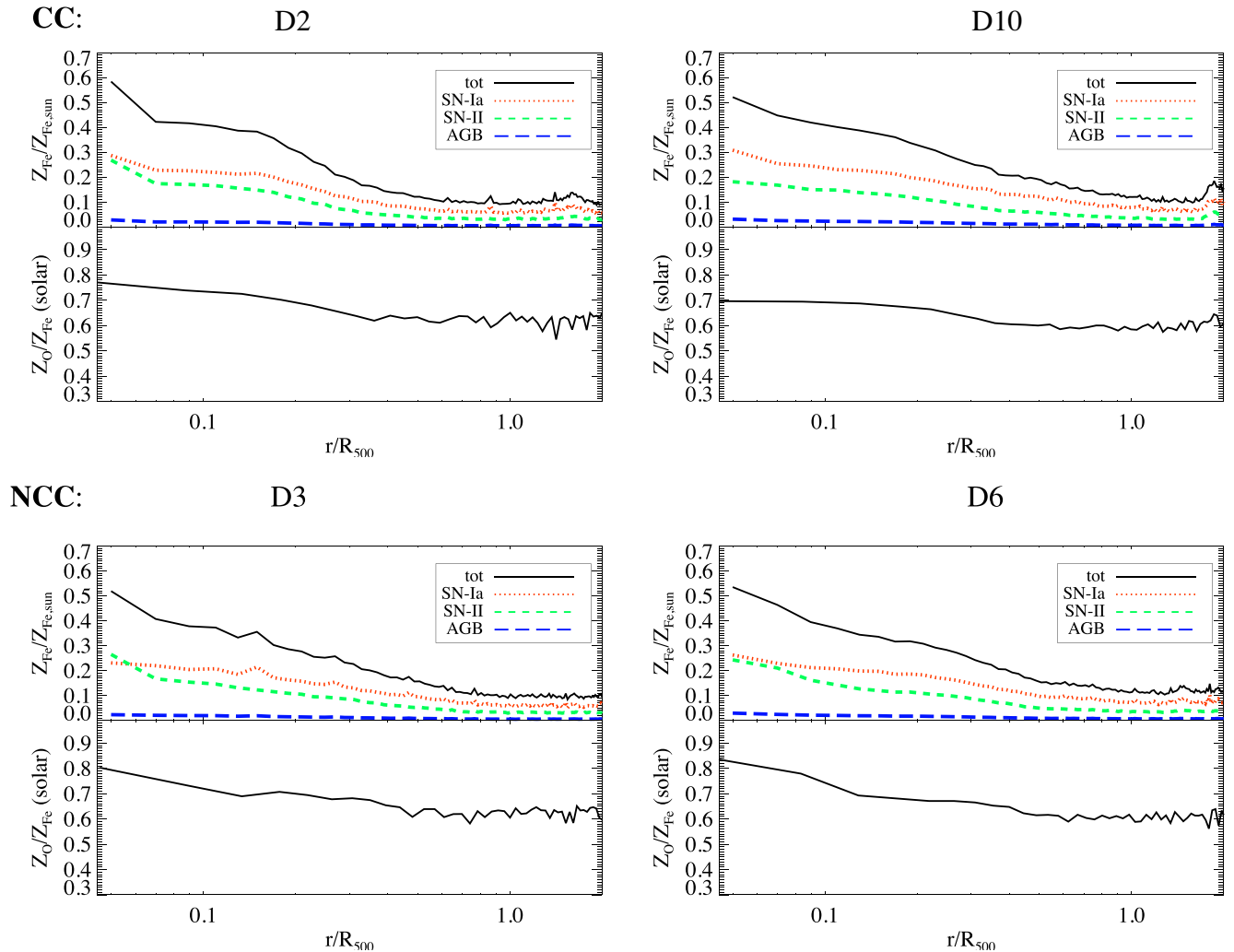


Figure 14. Upper insets: MW radial profiles of Fe abundance at $z = 0$, differentiating the different enrichment sources: SNIa (magenta dotted line), SNII (blue, dashed line) and AGB (green long-dashed line). For comparison, also the total iron-abundance profile is shown (black, solid line). Lower insets: MW radial profile of the observable tracer, O/Fe, of the relative contribution between SNII and SNIa products. In the upper row the clusters are CC systems (D2 and D10, from left to right respectively), while the two clusters in the lower row are NCC (D3 and D6).

6 TRACING THE CONTRIBUTION FROM DIFFERENT ENRICHMENT SOURCES

We investigate in this section the effective contributions to the ICM metal enrichment by the three stellar sources explicitly traced in the simulations, namely SNIa, SNII and AGB stars. As a study case, we restrict the analysis to four representative clusters, selected at $z = 0$ to be two massive haloes and two smaller systems, and for each pair of clusters we choose one CC and one NCC cluster.

Considering iron as a typical tracer of ICM metallicity, we explore the $z = 0$ Fe abundance profile cluster by cluster, computed for the three aforementioned enrichment sources separately. This is shown in Fig. 14 (upper inset in each panel). From the comparison against the oxygen-to-iron abundance ratio, reported in the lower inset of each panel, we can investigate directly the capability of this observable quantity to unveil the relative contribution of SNII and SNIa to the ICM enrichment.

From the Fe profiles in Fig. 14, we confirm that AGB stars basically release an almost null amount of Fe, except for the contribution due to the iron locked within the stars that form from gas that was previously enriched with it. Inspecting the four sets of profiles, we

also see that there is a general tendency for the SNIa and SNII Fe-profiles to be similarly flat in the cluster outskirts. This resemblance is the origin of the flatness of the O/Fe profile in the outer region of the clusters, pointing to a similarly homogeneous distribution of the metal products from the two enrichment channels. Towards the central regions, instead, the iron abundance profile corresponding to SNII enrichment typically presents a steepening with respect to the SNIa one, which is overall higher but flatter throughout the entire radial range. This trend is mirrored by the typical increase of the O/Fe abundance ratio in the cluster innermost region.

Taking advantage of the information in the simulations, we can actually directly compute the contribution from SNII and SNIa to the total ICM metal content. In Fig. 15, we present in the upper inset of each panel the ratio between the mass of metals produced by SNII and that produced by SNIa, $M_Z(II)/M_Z(Ia)$, as a function of radius. This is compared as well to the observational O/Fe tracer.

At $z = 0$, the shape of the two profiles is very similar and both indicators agree in a flat relative distribution of SNII to SNIa metal enrichment outside $0.1\text{--}0.2 R_{500}$. The main difference between the two indicators is given by the larger scatter in the $M_Z(II)/M_Z(Ia)$

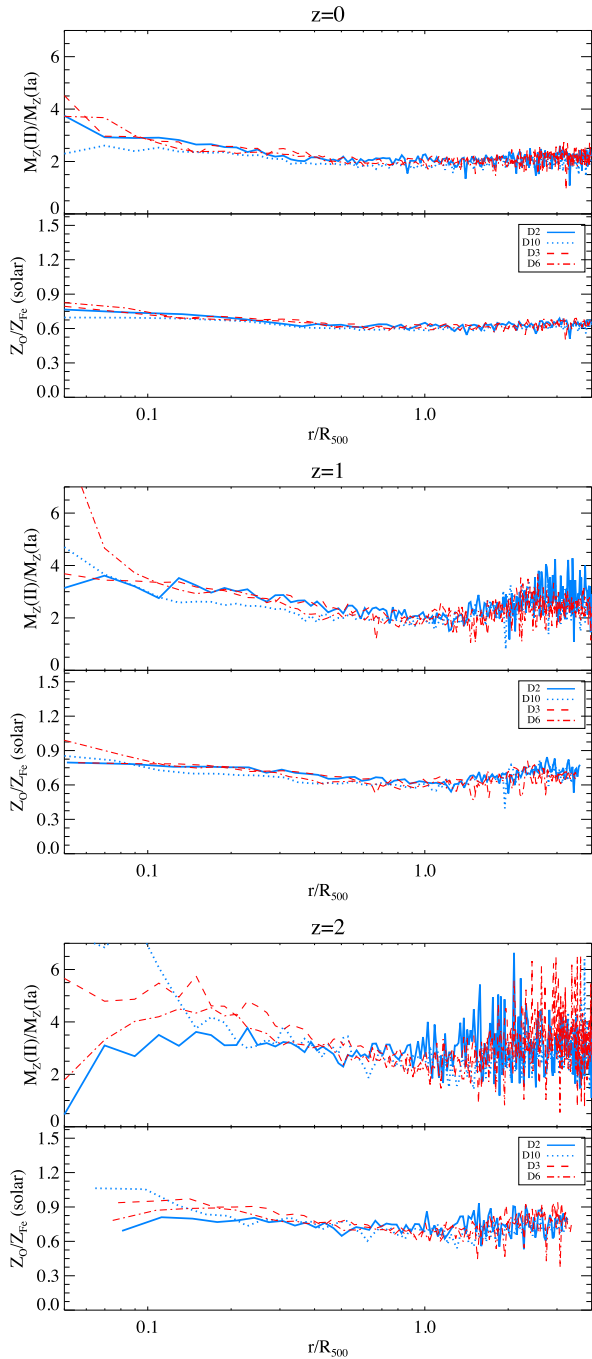


Figure 15. In each panel, we show the comparison of (i) the ratio between the metals released by SNII and SNIa (top); and (ii) the MW radial profile of the O/Fe abundance ratio. From top to bottom, the redshifts shown are $z = 0$, $z = 1$ and $z = 2$, respectively. As in the legend, the different lines refer to the four clusters considered, with blue and red marking the CC and NCC classification done at $z = 0$.

ratio, especially in the central part and in the outermost regions. This is mainly due to the difference in the actual relative contributions probed: the iron metallicity considered within the O/Fe abundance ratio is in fact contributed by both SNII and SNIa, even though with different proportions (as seen in Fig. 14). We verified that the profiles of $M_Z(II)/(M_Z(II) + M_Z(Ia))$ present a significantly lower scatter, and essentially show a strong similarity with the O/Fe profiles. By

examining the evolution of these profiles, shown in the central and bottom panels, we note that there is no particular trend associated with the classification of the clusters as CC or NCC at $z = 0$.

Independently of the enhancement previously discussed for the $M_Z(II)/M_Z(Ia)$ case, we find that the scatter among the different clusters augments in both indicators at higher redshift, especially within $0.3\text{--}0.4 R_{500}$, where differences between the specific star formation history of the clusters become more important. At large distances from the cluster centre the profiles tend to become also noisier, which is likely due to the more clumpy distribution of the metals at early times with respect to the more homogeneous one at $z = 0$, when mixing processes of the gas have had more time to be effective. At all redshifts, part of the noise that characterises the region outside R_{500} remains because those outer regions are more prominently affected by the presence and the infall of smaller substructures.

Overall, we find that in the cluster outskirts (outside of $0.3\text{--}0.4 R_{500}$) the relative contribution of SNII and SNIa to the enrichment does not change significantly from $z = 2$ to $z = 0$, except for a further flattening of the profiles and a decrease of the scatter due to the progressive contribution of late-time enrichment by SNIa.

7 SUMMARY AND CONCLUSION

In this paper we have presented an analysis of the ICM chemical properties for a sample of 29 clusters from zoom-in, cosmological, hydrodynamical simulations. As a first step, we compare the results at $z = 0$ with observational findings available from the literature, obtained with X-ray telescopes such as *Chandra*, *XMM-Newton* and *SUZAKU*. We subsequently explore the role of different feedback sources and enrichment channels on the distribution of the metal-rich ICM at $z = 0$ and at different epochs through the cosmic time, by comparing two runs of the simulations, with and without the treatment of AGN feedback (AGN and CSF runs, respectively).

The main results of this work are summarized in the following.

- (i) In our set of simulations, able to produce the observed diversity of central properties that discriminate between CC and NCC systems, we also recover the observed anti-correlation between entropy and metallicity in cluster cores at $z = 0$. Considering the intrinsic (MW and three-dimensional) quantities, such anti-correlation is instead weaker than observed and tends to fade with increasing redshift.
- (ii) We find overall good agreement between radial profiles of ICM metallicity and abundance ratios predicted by the simulations and available observational data at $z = 0$.
- (iii) We find relatively flat abundance ratio profiles in cluster outskirts ($r \gtrsim 0.1\text{--}0.2 R_{180}$) out to very large cluster-centric distances, both in the EW projected profiles and in the intrinsic (MW, 3D) ones.
- (iv) The level of enrichment in the intermediate and outer regions is already established at $z \sim 1\text{--}2$ and does not depend on the cool-core-ness of the halo at any times.
- (v) Overall, we find no evidence for significant metallicity evolution of the hot gas in the whole sample, between $z = 2$ and $z = 0$; instead, we find an increase of the metal mass in both gas and stars, with an increasing metallicity of the star-forming gas component, in the innermost region.
- (vi) The homogeneous distribution out to large radii of SNII products (e.g. oxygen), typically associated with star-forming regions, is mainly driven by the high-redshift AGN feedback, which

favours the spatial distribution and mixing of already enriched gas in the small substructures that eventually form the cluster.

Our findings strongly support the idea that the wide spreading of metal-enriched gas, which turns into the remarkably homogeneous enrichment found in the outskirts of low-redshift clusters, has happened mostly at early times ($z > 2-3$), during – but even before – the epoch of maximal star formation and AGN activity (see also recent results by Ezer et al. 2017). In particular, we found that the early AGN feedback acting on high-redshift ($z > 2$) small haloes, characterized by shallower potential wells, is particularly efficient in spreading the metal-enriched gas out to the halo virial radius and well beyond. This is the crucial step to distribute the enriched gas over large regions, even before the merging of the sub-structures on to the main cluster. This explains the homogeneous metallicity distribution observed at large cluster-centric distances at $z \lesssim 2$ down to $z = 0$, even in the case of SNII elements like oxygen, which is typically associated with recent star formation episodes. In this framework, the flat proportion between SNII and SNIa products further indicates that both populations of SN contributed to that early enrichment, (see also recent observational results obtained with SUZAKU by Mernier et al. 2017), and their relative contribution to the total mass of metals produced does not significantly change from $z = 2$ to $z = 0$.

These results essentially confirm the observational findings obtained so far by exploring the outer volume ($R_{500} \lesssim r \lesssim R_{200}$) of massive clusters in the local Universe (e.g. with SUZAKU; Fujita et al. 2008; Werner et al. 2013; Simionescu et al. 2015). Nevertheless, due to their low surface brightness, cluster outskirts still remain a largely un-explored territory for studies aimed at precisely estimating heavy elements abundances, which are on the contrary much better constrained in the innermost regions (e.g. de Plaa et al. 2007; Tamura et al. 2009; de Plaa 2013; Mernier et al. 2016a,b). Beyond the innermost regions, in fact, observational data are mostly limited in their statistical quality, which makes it very difficult to put tight constraints on the ICM metallicity. The thermodynamical structure and multi-phases of the ICM at large radii, typically beyond $0.2-0.4 R_{180}$, are poorly known and leave us with substantial uncertainties about a major portion of the ICM content. In fact, at intermediate and large cluster radii observations can be strongly contaminated by the background (see Molendi et al. 2016, for a dedicated study). In order to place tighter constraints on metal abundances in the periphery of clusters, next-generation X-ray missions with high spectral resolution and large effective area, such as *Athena*¹⁰ (Nandra et al. 2013), are definitely needed. This will substantially improve our understanding of the origin of the metal-rich gas (Ettori et al. 2013), by investigating the regions where the accretion and mixing processes are still ongoing. Also, such observational advancements will allow us to push the study of the ICM chemical properties out to higher redshifts (Pointecouteau et al. 2013), closer to the epoch when the bulk of the enrichment happened.

From the numerical point of view, state-of-the-art simulations, like those employed for the present analysis, managed to successfully model, for the first time, the thermal properties as well as the radial distribution of the heavy elements in the ICM, from the core region out to the boundary of low-redshift massive clusters. Nevertheless, we also found interesting discrepancies between predictions from simulations and observations, for instance concerning the evolution of the typical metallicity within the core of the clus-

ters. To further explore this issue, simulations with higher resolution and larger cluster samples are required, so that the relation between central entropy and metallicity can be investigated for statistically significant samples of CC and NCC, up to high redshifts. Furthermore, the possibility to track the origin of the metals in the ICM, both spatially and in terms of enrichment sources (e.g. SNII, SNIa, AGB stars), can pave the way for a number of focused studies: on the relation between specific feedback sources and enrichment channels; on the origin in space and time of the gas enriched by a specific stellar source and localized in the outskirts of clusters at $z = 0$; on the dynamical mixing of specific metal species depending on the sources that produced them.

As a final remark, we note that additional mechanisms connected to the interplay between BH accretion and ICM properties (such as kinetic feedback and inflation of bubbles of gas due to jets associated with the AGN, or possible effects of magnetic fields) as well as metal diffusion and depletion of heavy elements due to dust formation, that are still not included in our simulations, might play an important role in shaping the distribution of the metal-rich gas, especially in the outskirts.

ACKNOWLEDGEMENTS

The authors would like to thank S. Molendi, A. Simionescu and N. Werner for useful discussions, V. Springel for allowing us to access the developer version of the GADGET code and L. Steinborn for providing access to the improved AGN feedback model. Also, we thank the anonymous referee for constructive comments on the paper that helped in improving the presentation of our results. We acknowledge financial support from PIIF-GA- 2013-627474, NSF AST-1210973, PRIN-MIUR 201278X4FL, PRIN-INAF 2012 ‘The Universe in a Box: Multi-scale Simulations of Cosmic Structures’, the INFN INDARK grant, ‘Consorzio per la Fisica’ of Trieste, CONICET-Argentina, FonCyT. Simulations have been carried out using Flux HPC Cluster at the University of Michigan, Galileo at CINECA (Italy), with CPU time assigned through ISCRA proposals and an agreement with the University of Trieste. We also acknowledge PRACE for awarding us access to resource ARIS based in Greece at GRNET, through the DECI-13 PRACE proposal. The post-processing has been performed using the PICO HPC cluster at CINECA through our expression of interest. SP also acknowledges support by the *Spanish Ministerio de Economía y Competitividad* (MINECO, grants AYA2013-48226-C3-2-P and AYA2016-77237-C3-3-P and the Generalitat Valenciana (grant GVACOMP2015-227). DF acknowledges financial support from the Slovenian Research Agency (research core funding No. P1-0188). MG is supported by NASA through *Einstein* Postdoctoral Fellowship Award Number PF-160137 issued by the *Chandra* X-ray Observatory Center, which is operated by the SAO for and on behalf of NASA under contract NAS8-03060.

REFERENCES

- Anders E., Grevesse N., 1989, *Geochim. Cosmochim. Acta*, 53, 197
- Andreon S., 2012, *A&A*, 546, A6
- Baldi A., Ettori S., Mazzotta P., Tozzi P., Borgani S., 2007, *ApJ*, 666, 835
- Baldi A., Ettori S., Molendi S., Balestra I., Gastaldello F., Tozzi P., 2012, *A&A*, 537, A142
- Balestra I., Tozzi P., Ettori S., Rosati P., Borgani S., Mainieri V., Norman C., Viola M., 2007, *A&A*, 462, 429
- Beck A. M. et al., 2016, *MNRAS*, 455, 2110
- Biffi V. et al., 2016, *ApJ*, 827, 112

¹⁰ <http://www.the-athena-x-ray-observatory.eu>

- Böhringer H., Werner N., 2010, *A&AR*, 18, 127
- Böhringer H., Matsushita K., Churazov E., Finoguenov A., Ikebe Y., 2004, *A&A*, 416, L21
- Bonafede A., Dolag K., Stasyszyn F., Murante G., Borgani S., 2011, *MNRAS*, 418, 2234
- Borgani S., Fabjan D., Tornatore L., Schindler S., Dolag K., Diaferio A., 2008, *Space Sci. Rev.*, 134, 379
- Bryan G. L., Norman M. L., 1998, *ApJ*, 495, 80
- Chabrier G., 2003, *PASP*, 115, 763
- Churazov E., Brüggner M., Kaiser C. R., Böhringer H., Forman W., 2001, *ApJ*, 554, 261
- Cora S. A., Tornatore L., Tozzi P., Dolag K., 2008, *MNRAS*, 386, 96
- De Grandi S., Molendi S., 2001, *ApJ*, 551, 153
- De Grandi S., Ettori S., Longhetti M., Molendi S., 2004, *A&A*, 419, 7
- de Plaa J., 2013, *Astron. Nachr.*, 334, 416
- de Plaa J., Werner N., Bleeker J. A. M., Vink J., Kaastra J. S., Méndez M., 2007, *A&A*, 465, 345
- Dolag K., Hansen F. K., Roncarelli M., Moscardini L., 2005, *MNRAS*, 363, 29
- Ettori S. et al., 2013, preprint ([arXiv:e-prints](#))
- Ettori S., Baldi A., Balestra I., Gastaldello F., Molendi S., Tozzi P., 2015, *A&A*, 578, A46
- Ezer C., Bulbul E., Nihal Ercan E., Smith R. K., Bautz M. W., Loewenstein M., McDonald M., Miller E. D., 2017, *ApJ*, 836, 110
- Fabjan D., Tornatore L., Borgani S., Saro A., Dolag K., 2008, *MNRAS*, 386, 1265
- Fabjan D., Borgani S., Tornatore L., Saro A., Murante G., Dolag K., 2010, *MNRAS*, 401, 1670
- Finoguenov A., David L. P., Ponman T. J., 2000, *ApJ*, 544, 188
- Finoguenov A., Sanderson A. J. R., Mohr J. J., Bialek J. J., Evrard A., 2010, *A&A*, 509, A85
- Fujita Y., Tawa N., Hayashida K., Takizawa M., Matsumoto H., Okabe N., Reiprich T. H., 2008, *PASJ*, 60, S343
- Gaspari M., Melioli C., Brighenti F., D'Ercole A., 2011a, *MNRAS*, 411, 349
- Gaspari M., Brighenti F., D'Ercole A., Melioli C., 2011b, *MNRAS*, 415, 1549
- Haardt F., Madau P., 2001, in Neumann D. M., Tran J. T. V., eds, *Clusters of Galaxies and the High Redshift Universe Observed in X-rays*. CEA, Saclay, p. 64
- Karakas A., Lattanzio J. C., 2007, *Publ. Astron. Soc. Aust.*, 24, 103
- Kelly B. C., 2007, *ApJ*, 665, 1489
- Kirkpatrick C. C., McNamara B. R., 2015, *MNRAS*, 452, 4361
- Kravtsov A. V., Borgani S., 2012, *ARA&A*, 50, 353
- Leccardi A., Molendi S., 2008, *A&A*, 487, 461
- Leccardi A., Rossetti M., Molendi S., 2010, *A&A*, 510, A82
- McCarthy I. G. et al., 2010, *MNRAS*, 406, 822
- McCarthy I. G., Schaye J., Bower R. G., Ponman T. J., Booth C. M., Dalla Vecchia C., Springel V., 2011, *MNRAS*, 412, 1965
- McDonald M. et al., 2016, *ApJ*, 826, 124
- Martizzi D., Hahn O., Wu H. Y., Evrard A. E., Teyssier R., Wechsler R. H., 2016, *MNRAS*, 459, 4408
- Matsushita K., Sato T., Sakuma E., Sato K., 2013, *PASJ*, 65, 10
- Maughan B. J., Jones C., Forman W., Van Speybroeck L., 2008, *ApJS*, 174, 117
- Mernier F., de Plaa J., Pinto C., Kaastra J. S., Kosec P., Zhang Y. Y., Mao J., Werner N., 2016a, *A&A*, 592, A157
- Mernier F. et al., 2016b, *A&A*, 595, A126
- Mernier F. et al., 2017, *A&A*, preprint ([arXiv:1703.01183](#))
- Molendi S., Eckert D., De Grandi S., Ettori S., Gastaldello F., Ghizzardi S., Pratt G. W., Rossetti M., 2016, *A&A*, 586, A32
- Mushotzky R., Loewenstein M., Arnaud K. A., Tamura T., Fukazawa Y., Matsushita K., Kikuchi K., Hatsukade I., 1996, *ApJ*, 466, 686
- Nandra K. et al., 2013, preprint ([arXiv:e-prints](#))
- Padovani P., Matteucci F., 1993, *ApJ*, 416, 26
- Planelles S., Borgani S., Fabjan D., Killedear M., Murante G., Granato G. L., Ragone-Figueroa C., Dolag K., 2014, *MNRAS*, 438, 195
- Planelles S., Schleicher D. R. G., Bykov A. M., 2016a, *Multi-scale Structure Formation and Dynamics in Cosmic Plasmas: Space Sciences Series of ISSI*, Vol. 51. Springer Science+Business Media, New York, p. 93
- Planelles S. et al., 2016b, preprint ([arXiv:e-prints](#))
- Pointecouteau E. et al., 2013, preprint ([arXiv:e-prints](#))
- Rasia E., Mazzotta P., Bourdin H., Borgani S., Tornatore L., Ettori S., Dolag K., Moscardini L., 2008, *ApJ*, 674, 728
- Rasia E. et al., 2015, *ApJ*, 813, L17
- Rebusco P., Churazov E., Böhringer H., Forman W., 2005, *MNRAS*, 359, 1041
- Rebusco P., Churazov E., Böhringer H., Forman W., 2006, *MNRAS*, 372, 1840
- Romano D., Karakas A. I., Tosi M., Matteucci F., 2010, *A&A*, 522, A32
- Rossetti M., Eckert D., Cavalleri B. M., Molendi S., Gastaldello F., Ghizzardi S., 2011, *A&A*, 532, A123
- Sakuma E., Ota N., Sato K., Sato T., Matsushita K., 2011, *PASJ*, 63, S979
- Sato K., Matsushita K., Ishisaki Y., Yamasaki N. Y., Ishida M., Sasaki S., Ohashi T., 2008, *PASJ*, 60, S333
- Simionescu A., Werner N., Finoguenov A., Böhringer H., Brüggner M., 2008, *A&A*, 482, 97
- Simionescu A., Werner N., Böhringer H., Kaastra J. S., Finoguenov A., Brüggner M., Nulsen P. E. J., 2009, *A&A*, 493, 409
- Simionescu A., Werner N., Urban O., Allen S. W., Ichinohe Y., Zhuravleva I., 2015, *ApJ*, 811, L25
- Springel V., 2005, *MNRAS*, 364, 1105
- Springel V., Hernquist L., 2003, *MNRAS*, 339, 289
- Steinborn L. K., Dolag K., Hirschmann M., Prieto M. A., Remus R. S., 2015, *MNRAS*, 448, 1504
- Tamura T. et al., 2009, *ApJ*, 705, L62
- Thielemann F. K. et al., 2007, *Progress Part. Nucl. Phys.*, 59, 74
- Tornatore L., Borgani S., Matteucci F., Recchi S., Tozzi P., 2004, *MNRAS*, 349, L19
- Tornatore L., Borgani S., Dolag K., Matteucci F., 2007, *MNRAS*, 382, 1050
- Truong N. et al., 2016, preprint ([arXiv:e-prints](#))
- Villaescusa-Navarro F. et al., 2016, *MNRAS*, 456, 3553
- Werner N., Urban O., Simionescu A., Allen S. W., 2013, *Nature*, 502, 656
- Wiersma R. P. C., Schaye J., Smith B. D., 2009, *MNRAS*, 393, 99
- Woosley S. E., Weaver T. A., 1995, *ApJS*, 101, 181

APPENDIX A: CC IN THE CSF SIMULATION?

Despite the fact that the majority of the clusters in the CSF run appear to be NCC clusters, as well known from previous analyses,

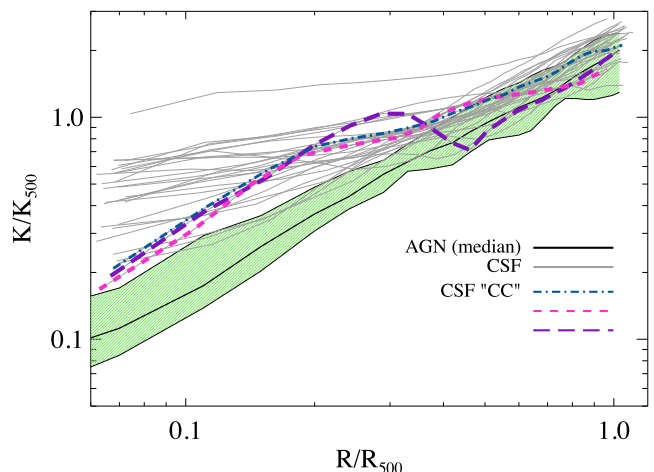


Figure A1. Comparison between the median entropy profile of the AGN CC clusters (black solid line and shaded area) and the single entropy profiles for the CSF sample (grey thin lines). Marked in coloured thick lines are the three clusters with $\sigma < 0.55$.

we note from the bottom panel in Fig. 2 that five clusters of our CSF sample have 2D pseudo-entropy below the $\sigma = 0.55$ threshold, and therefore could be classified as CC systems. We inspected these five clusters in more detail. Out of these, two clusters – those close to the threshold line – are not confirmed to be real CC systems when the value of the pseudo-entropy σ is computed intrinsically for the three-dimensional spherical ‘IN’ region. This is also confirmed by the visual inspection of their entropy profiles and maps.

The three remaining clusters with the lowest values of σ in the projected EW case present a value of the pseudo-entropy in the core region that is lower than 0.55 even when the 3D MW estimate

is considered. Nevertheless, these clusters show irregular entropy profiles that are generally higher and less smooth than the typical profiles of the CC systems obtained in the AGN sample, which are instead in good agreement with observations Rasia et al. (2015). The three objects are highlighted in Fig. A1, where the other individual entropy profiles of the CSF clusters are marked in thin grey lines and the median entropy profile of CC systems in the AGN sample is also reported (black line with shaded area).

This paper has been typeset from a $\text{\TeX}/\text{\LaTeX}$ file prepared by the author.